Maximum Bound Principle and Non-negativity Preserving ETD Schemes for a Phase Field Model of Prostate Cancer Growth with Treatment

Qiumei Huang[a], Zhonghua Qiao[b], Huiting Yang[a,*]

[a] *College of Mathematics, Faculty of Science, Beijing University of Technology, Beijing 100875, China*
[b] *Department of Applied Mathematics, The Hong Kong Polytechnic University, Hung Hom, Kowloon, Hong Kong*

Abstract

Prostate cancer (PCa) is a significant global health concern that affects the male population. In this study, we present a numerical approach to simulate the growth of PCa tumors and their response to drug therapy. The approach is based on a previously developed model, which consists of a coupled system comprising one phase field equation and two reaction-diffusion equations. To solve this system, we employ the fast second-order exponential time differencing Runge–Kutta (ETDRK2) method with stabilizing terms. This method is a decoupled linear numerical algorithm that preserves three crucial physical properties of the model: a maximum bound principle (MBP) on the order parameter and non-negativity of the two concentration variables. Our simulations allow us to predict tumor growth patterns and outcomes of drug therapy over extended periods, offering valuable insights for both basic research and clinical treatments.

Keywords: Prostate cancer tumor growth, Drug therapy, Phase field equation, Exponential time differencing Runge–Kutta, Maximum bound principle, Non-negativity

1. Introduction

According to the Cancer Statistics 2023 [32], prostate cancer (PCa) is a prevalent malignancy in males, with the highest incidence rate of new cases and ranking as the second leading cause of cancer-related deaths among men in the United States. Therefore, there is an urgent need for continuous research efforts focused on PCa to develop more effective prevention and treatment strategies.

Currently, diagnostic techniques for PCa include digital rectal examination, ultrasound examination, magnetic resonance imaging, and prostate-specific antigen (PSA) testing. Among these methods, the PSA test is widely used in the screening and diagnosis of PCa due to its simplicity, reliability, non-invasiveness, and cost-effectiveness. Lilja et al. [19] have provided an extensive elucidation of the concept, measurement methodologies, and clinical significance of serum PSA and PSA dynamics. PSA is primarily produced by prostate cells as a protein present in semen and is also found in small quantities in the bloodstream. In the presence of prostate cancer, damaged prostate ducts can lead to elevated PSA levels in the blood. Therefore, the PSA test is commonly used as an

*Corresponding author

Email addresses: qmhuang@bjut.edu.cn (Qiumei Huang), zqiao@polyu.edu.hk (Zhonghua Qiao), yanghuiting2021@emails.bjut.edu.cn (Huiting Yang)

early screening tool for prostate cancer. PSA dynamics, which evaluates the growth rate and treatment efficacy of PCa based on the trend of serum PSA values, plays a crucial role in PCa research. Despite the ongoing controversy within the medical community regarding PSA testing, primarily due to limitations such as high false positive rates, recent research [32] indicates that the annual increase rate of PCa incidence has gradually decreased in recent years, partially attributed to a greater number of individuals utilizing PSA testing tools for routine check-ups. In recent years, significant advancements in the treatment of PCa, such as chemotherapy, targeted therapy, and immunotherapy, have provided new avenues and renewed hope for patients. K.J. Pienta and D.C. Smith [27] emphasized that chemotherapy is currently a primary approach for managing advanced PCa. However, while conventional chemotherapy regimens can reduce tumor burden, they are often insufficient to eradicate late-stage disease. Therefore, future efforts in cancer treatment will focus on combining traditional chemotherapy with novel drugs that target specific signaling pathways and investigating the intricate interplay between cancer cells and the host environment.

Numerical simulation has gained prominence as a cost-effective, resource-efficient, and reproducible method for studying tumor growth. It has become an invaluable tool for physicians to gain a deeper understanding of tumor morphology, structure, and invasive characteristics. Wise et al. [37] proposed a three-dimensional multiscale model utilizing Cahn-Hilliard and reaction-diffusion equations to describe multispecies tumor growth and tumor-induced angiogenesis. They employed adaptive nonlinear multigrid techniques for spatial discretization and second-order Crank-Nicholson schemes for time discretization. Mohammadi and Dehghan [24] presented a numerical approach based on the element-free Galerkin method and second-order semi-implicit backward differentiation formula for time discretization to solve Cahn-Hilliard equations and four-species tumor growth equations. Lu et al. [22] investigated the impact of necrotic cores and vascular nutrient supply on tumor morphology using a two-dimensional mathematical model with a sharp interface. Their model utilized the spectral accuracy boundary integral method (BIM) and a second-order semi-implicit time-stepping method for simulating tumor morphology. Shen et al. [31] employed the scalar auxiliary variable (SAV) method for nonlinear term handling, semi-implicit difference schemes for time discretization, and Fourier-spectral methods for spatial discretization. They developed an efficient algorithm for energy dissipation and mass conservation in a diffusion-interface tumor growth model. Thomas J.R. Hughes, Hector Gomez and their collaborators have made notable contributions to PCa simulations by incorporating clinical medical data into models that consider various subtypes and individual patient differences in disease development and progression. Their research provides valuable insights into treatment strategies and drug selection in the field of PCa simulations. Lorenzo et al. [21] proposed a personalized tissue-level model for PCa using the phase field method and diffusion-reaction equations. They utilized isogeometric analysis (IGA) and the generalized-α method for temporal discretization, providing new insights into the mechanisms behind tumor morphology changes. Building upon this model, Mohammadi et al. [25] employed a radial basis function-generated finite difference (RBF-FD) scheme for spatial discretization and the semi-implicit backward differentiation formula of first-order (SBDF1) for temporal discretization. Lorenzo et al. [20] developed a patient-specific, tissue-level mathematical model to qualitatively investigate the mechanical interaction between PCa and benign prostatic hyperplasia. They employed a staggered numerical method with isogeometric spatial discretization and generalized-α temporal integration. The Newton-Raphson algorithm was utilized for

equation linearization, and within each iteration, the GMRES algorithm with a diagonal preconditioner was employed to solve the linear system. In another study, Lorenzo et al. [3] developed a phase field model to simulate PCa growth and investigate the response to chemotherapy, antiangiogenic therapy, and combined therapy, using similar numerical methods as previous studies. This study provides strong support for the design of personalized chemotherapeutic protocols for PCa patients. For this PCa growth model, Narimani et al. [26] utilized a generalized form of the direct radial basis function partition of unity (D-RBF-PU) method for spatial discretization and the SBDF1 algorithm for time discretization. The resulting discretized algebraic equations were solved using the biconjugate gradient stabilized (BiCGSTAB) method with a zero-fill incomplete lower-upper (ILU) preconditioner. Despite the impressive contributions of these studies, numerical simulations did not take into account the physical properties of boundedness of the order parameter and the non-negative nature of the two concentration variables.

In numerical computations, it is customary to adhere to the maximum bound principle (MBP) for both the mathematical model and its discrete form. The MBP ensures that the numerical solution remains within the function's domain, preventing computational errors such as overflow and yielding physically plausible solutions. Du et al. [4, 5] established an abstract framework for analyzing the MBPs of semilinear parabolic equations and proposed unconditionally MBP-preserving first-order exponential time differencing (ETD1) and second-order exponential time differencing Runge–Kutta (ETDRK2) methods. They also employed fast fourier transform (FFT) technology to enhance computational efficiency. Ju et al. [16] investigated high-order integrating factor Runge–Kutta (IFRK) algorithms that preserve the MBP for semilinear parabolic equations. The efficiency of these algorithms was validated through numerical simulations of long-term evolution in two and three dimensions. For readers seeking a more comprehensive understanding of the maximum boundary principle preserving schemes, references [2, 7, 11, 12, 13, 14, 15, 18, 30, 33] offer valuable resources for further exploration.

In this study, we utilize the second-order exponential time differencing Runge-Kutta (ETDRK2) method for time discretization and the second-order central difference method for spatial discretization in order to solve the phase-field model of tumor growth. Our algorithm is characterized by two significant features. Firstly, it employs a decoupled and explicit scheme, which can be efficiently solved using fast discrete cosine transform (DCT) and discrete sine transform (DST) solvers. This approach is more efficient compared to the nonlinear solvers employed in the original study [3]. Secondly, our algorithm ensures the preservation of three essential physical properties. These properties are manifested at the PDE level of the model, but have not been considered at the numerical level in other existing reference papers.

This paper is structured as follows. In Section 2, we review the mathematical models proposed by Colli et al. [3] for tumor growth and drug treatment. In Section 3, we present the ETD1 and ETDRK2 algorithms for the coupled model. These algorithms ensure the preservation of the discrete MBP for the order parameter and the discrete non-negativity property for the concentration variables. In Section 4, we conduct a series of numerical simulations, including the simulation of tumor growth without treatment and after treatment, in order to validate and analyze the model. Finally, in Section 5, we summarize the main achievements of this study and discuss potential future research directions.

2. Model Review

In this section, we provide an overview of the mathematical model proposed by Colli et al. [3] for describing the growth of PCa and its response to chemotherapy and antiangiogenic therapy. The model incorporates a phase field equation to capture tumor dynamics and considers the concentrations of critical nutrients σ and prostate-specific antigen (PSA) p in the prostate tissue. The dynamics of these nutrient concentrations and PSA levels are represented by reaction-diffusion equations.

2.1. Tumor Dynamics

In this model, an order parameter ϕ is introduced to describe the temporal evolution of the tumor's location and geometry. Within the healthy tissue, the value of ϕ is approximately 0, indicating the absence of tumor cells. In the tumor region, on the other hand, ϕ is approximately 1, representing the presence of tumor cells. The transition from 0 to 1 of the order parameter ϕ occurs smoothly across a diffusion interface.

The tumor dynamics is described by the following equation [38]:

$$\phi_t = -M\left(-l^2\Delta\phi + \frac{\partial G}{\partial \phi}(\phi, \sigma, u)\right),$$

where M and l are positive real constants representing the tumor mobility and interface width, respectively, and

$$G(\phi, \sigma, u) = F(\phi) - h(\phi)\left(m(\sigma) - m_{\text{ref}}u\right).$$

Here, $F(\phi)$ and $h(\phi)$ denote the double-well potential function and interpolation function, respectively, which are often defined as follows:

$$F(\phi) = \phi^2(1-\phi)^2, \quad h(\phi) = \phi^2(3-2\phi).$$

The net tumor proliferation rate is given by

$$m(\sigma) = m_{\text{ref}}\left(\frac{\rho + A}{2} + \frac{\rho - A}{\pi}\arctan\left(\frac{\sigma - \sigma_l}{\sigma_r}\right)\right). \tag{2.1}$$

In this equation, ρ and A represent the constant indices for proliferation and apoptosis, respectively. The nutrient concentration is represented by the reference value σ_r and the threshold value σ_l.

The function u represents the tumor-inhibiting effect of the cytotoxic drug docetaxel, which is commonly used in the clinical management of advanced prostate cancer [29]. The impact of the drug on tumor dynamics is assumed to be linearly dependent on its concentration [8, 10, 28]. Following drug administration, a decline in systemic drug concentration is observed to exhibit an exponential pattern, as described in references [1, 34]. Thus, the cytotoxic drug function can be described by the following equation:

$$u(t) = \sum_{i=1}^{n_c} \beta_c d_c e^{-\frac{t-T_{c,i}}{\tau_c}} \mathcal{H}\left(t - T_{c,i}\right), \tag{2.2}$$

where the Heaviside function $\mathcal{H}$ is employed as a switch to activate the drug's action. n_c denotes the number of chemotherapy cycles, β_c signifies the impact of cytotoxic chemotherapy on tumor dynamics per unit of drug dose administered, d_c represents the dose of docetaxel, $\{T_{c,i}\}_{i=1,\ldots,n_c}$ denotes the times at which the drug is administered, and τ_c stands for

the mean lifetime of docetaxel, i.e., the reciprocal of the exponential decay constant. In the modeling process of [3], the experimental and clinical data obtained for β_c guarantee the condition $|m(\sigma) - m_{\text{ref}}u| < \frac{1}{3}$. This condition implies that the function $G(\phi, \sigma, u)$ is a double-well potential with local minima at $\phi = 0$ and $\phi = 1$, which plays a pivotal role in our analysis.

Then the time evolution of the phase field variable is given by:

$$\phi_t = \lambda\Delta\phi - 2M\phi(1-\phi)\left[1 - 2\phi - 3\left(m(\sigma) - m_{\text{ref}}u\right)\right], \text{ in } Q_T := (0,T)\times\Omega, \tag{2.3}$$

where $\lambda = Ml^2$ denotes the diffusion coefficient of tumor cells and T denotes a final time. Ω is an open bounded subset of $\mathbb{R}^N (N \leq 3)$, with a sufficiently smooth boundary $\partial\Omega$.

2.2. Critical Nutrient Dynamics

Assuming that tumor growth is primarily influenced by the concentration of key nutrients σ (mainly composed of glucose), the following reaction-diffusion equation is employed to model nutrient dynamics:

$$\sigma_t = \eta\Delta\sigma + S_h(1-\phi) + (S_c - s)\,\phi - \left(\gamma_h(1-\phi) + \gamma_c\phi\right)\sigma, \text{ in } Q_T \tag{2.4}$$

where η represents the diffusion coefficient, S_h and S_c denote the nutrient supply rates in healthy tissue and cancerous tissue, respectively. The variable s represents the reduction in nutrient supply induced by antiangiogenic therapy. The parameters γ_h and γ_c represent the nutrient uptake rates in healthy and cancerous tissues, respectively.

The function $s(t)$ represents the antiangiogenic effect of the therapeutic agent bevacizumab, which is extensively studied for its potential in the treatment of prostate cancer [6, 23]. Analogous to the function $u(t)$, $s(t)$ can be mathematically described using the following formula:

$$s(t) = \sum_{i=1}^{n_a} \beta_a d_a e^{-\frac{t-T_{a,i}}{\tau_a}} \mathcal{H}\left(t - T_{a,i}\right).$$

In the above equations, the variable n_a denotes the number of antiangiogenic treatment cycles, β_a signifies the impact of antiangiogenic therapy on nutrient supply per unit of drug dose administered, d_a represents the dose of bevacizumab, $\{T_{a,i}\}_{i=1,\ldots,n_a}$ denotes the times at which the drug is administered, and τ_a represents the mean lifetime of bevacizumab. In the formulation of the original model [3], it is ensured that S_h, S_c are nonnegative, and $0 \leq s \leq S_c$, which will be utilized in subsequent parts of our analysis.

2.3. Tissue PSA Dynamics

The Prostate-specific antigen (PSA) test is primarily used for screening PCa by measuring PSA levels in the blood. Both host tissue and tumors produce PSA, but tumors produce PSA at a much faster rate than host tissue. Similar to nutrient dynamics, a reaction-diffusion equation is employed to describe PSA dynamics [21]:

$$p_t = D\Delta p - \gamma_p p + \alpha_h(1-\phi) + \alpha_c\phi, \text{ in } Q_T, \tag{2.5}$$

where D and γ_p represent the diffusion coefficient and the natural decay rate, respectively. α_h and α_c denote the tissue-specific PSA production rates in host tissue and cancerous tissues, respectively.

Then the serum PSA P_S is given as the integral of the tissue PSA p over Ω:

$$P_s = \int_\Omega p d\boldsymbol{x}. \tag{2.6}$$

The volumes of tumor V_c and host tissue V_h can also be obtained by the following equations:

$$V_c = \int_\Omega \phi d\boldsymbol{x}, \quad V_h = \int_\Omega (1-\phi) d\boldsymbol{x}. \tag{2.7}$$

Presented below is Table 1, which encompasses all the parameters pertaining to tumor dynamics, nutrient dynamics, and tissue PSA dynamics.

Table 1: Parameter values involved in dynamics system [3].

Parameter	Notation	Value
Tumor Dynamics		
Tumor phase field diffusivity	λ	$640 \quad \mu\text{m}^2/\text{ day}$
Tumor mobility	M	$2.5 \quad 1/\text{ day}$
Net proliferation scaling factor	m_{ref}	$7.55 \cdot 10^{-2} \quad 1/\text{ day}$
Proliferation index	ρ	$8/15, \quad 1$
Apoptosis index	A	$-1/3, \quad -137/210$
Reference value of nutrient concentration	σ_r	$1/15$
Threshold value of nutrient concentration	σ_l	0.4
Mean lifetime of cytotoxic drug	τ_c	$5 \quad \text{day}$
Cytotoxic drug effect	β_c	$1.59 \cdot 10^{-2} \quad 1/\left(\text{mg}/\text{m}^2\right)$
Cytotoxic drug dose	d_c	$75 \quad \text{mg}/\text{m}^2$
Critical Nutrient Dynamics		
Nutrient diffusivity	η	$6.4 \cdot 10^4 \quad \mu\text{m}^2/\text{ day}$
Nutrient supply in healthy tissue	S_h	$2 \quad g/L/\text{ day}$
Nutrient supply in tumor tissue	S_c	$2.7, 3.125, 2.375 \quad g/L/\text{ day}$
Nutrient uptake by healthy tissue	γ_h	$2 \quad g/L/\text{ day}$
Nutrient uptake by tumor tissue	γ_c	$17, 18, 16 \quad g/L/\text{ day}$
Mean lifetime of antiangiogenic drug	τ_a	$30 \quad \text{day}$
Antiangiogenic drug effect	β_a	$0.04 \quad g/L/\text{ day} \;/\left(\text{mg}/\text{kg}\right)$
Antiangiogenic drug dose	d_a	$15 \quad \text{mg}/\text{kg}$
Tissue PSA Dynamics		
Tissue PSA diffusivity	D	$640 \quad \mu\text{m}^2/\text{ day}$
Healthy tissue PSA production rate	α_h	$1.712 \cdot 10^{-2} \quad \text{ng}/\text{mL}/\text{cc}/\text{ day}$
Tumoral tissue PSA production rate	α_c	$\alpha_c = 15\alpha_h$
Tissue PSA natural decay rate	γ_p	$0.274 \quad 1/\text{ day}$

2.4. Coupled System

Finally, we obtained a coupled governing system in Q_T:

$$\begin{aligned}
\phi_t &= \lambda\Delta\phi - 2M\phi(1-\phi)\left[1-2\phi-3\left(m(\sigma)-m_{\text{ref}}u\right)\right], \\
\sigma_t &= \eta\Delta\sigma + S_h(1-\phi) + (S_c - s)\,\phi - \left(\gamma_h(1-\phi)+\gamma_c\phi\right)\sigma, \\
p_t &= D\Delta p - \gamma_p p + \alpha_h(1-\phi) + \alpha_c\phi,
\end{aligned} \tag{2.8}$$

with the initial and boundary conditions

$$\begin{aligned}
&\phi(0) = \phi_0, \quad \sigma(0) = \sigma_0, \quad p(0) = p_0, \quad \text{in } \Omega, \\
&\phi = 0, \quad \frac{\partial\sigma}{\partial\mathbf{n}} = \frac{\partial p}{\partial\mathbf{n}} = 0, \quad \text{on } \Sigma_T := (0,T)\times\partial\Omega,
\end{aligned} \tag{2.9}$$

where $\mathbf{n}$ is the outer unit normal vector on the boundary.

In [3], the authors have provided a rigorous proof for the well-posedness of this model, i.e. its solution exists and is unique. Additionally, they have rigorously proven the following three important physical properties that the three variables, ϕ, σ, and p, must satisfy:

(i). The order parameter ϕ needs to be between 0 and 1, i.e., $\phi \in [0, 1]$.

(ii). The nutrient concentration needs to be non-negative and bounded, i.e., $0 \leq \sigma < \infty$.

(iii). The tissue PSA concentration needs to be non-negative and bounded, i.e., $0 \leq p < \infty$.

To solve this model, they used an isogeometric discretization based on the Galerkin method for space discretization. For time discretization, they used the generalized-α method and linearized the resulting nonlinear system of equations by the Newton-Raphson algorithm. However, the proposed algorithm is a coupled, implicit, and nonlinear scheme that requires iterative solving and does not preserve the three physical properties (i)-(iii) numerically.

Our main contribution of this paper is the design of a decoupled, linear, and explicit scheme, which makes our approach more intelligible and straightforward to implement. Additionally, by incorporating simple stabilizing constants, our scheme effortlessly preserves three essential physical properties, numerically. This innovative method not only enhances computational efficiency but also reinforces the physical realism of the numerical results.

3. Numerical Method

In this section, we construct numerical schemes satisfying the physical properties of (i) - (iii) which are based on the exponential time differencing method.

3.1. The Phase Field Equation of ϕ

3.1.1. Maximum Bound Principle of the Phase Field Equation

To ensure property (i), take the affine transform $\zeta(\theta) : \mathbb{R}^N \to \mathbb{R}^N (N \leq 3)$ defined by

$$\zeta(\theta) = \frac{1}{2}\theta + \frac{1}{2}, \quad \theta \in \mathbb{R}^N.$$

By letting $\psi = \zeta^{-1}(\phi)$, we can obtain a new equation about ψ:

$$\psi_t = \lambda\Delta\psi + M(1-\psi^2)[\psi + 3(m(\sigma) - m_{ref}u)], \quad \text{in } Q_T, \tag{3.1}$$

which satisfies the following relationships:

$$\phi = \frac{\psi + 1}{2}, \qquad \psi = 2\phi - 1, \tag{3.2}$$

with the following initial values and boundary conditions:

$$\begin{aligned} &\psi(0) = 2\phi_0 - 1, \quad \text{in } \Omega, \\ &\psi = 2\phi - 1 = -1, \quad \text{on } \Sigma_T := (0, T) \times \partial\Omega. \end{aligned} \tag{3.3}$$

Then we transform the problem of preserving the order parameter $\phi \in [0, 1]$ into preserving the order parameter $\psi \in [-1, 1]$.

Let us introduce a stabilizing constant $\kappa_1 > 0$ and rewrite (3.1) into the following equivalent form:

$$\psi_t(t, \boldsymbol{x}) + \mathcal{L}_{\kappa_1}\psi(t, \boldsymbol{x}) = \mathcal{N}_1[\psi](t, \boldsymbol{x}), \quad \text{in } Q_T, \tag{3.4}$$

where

$$\begin{aligned}
&\mathcal{L}_{\kappa_1} = -\lambda\Delta + \kappa_1\mathcal{I},\\
&\mathcal{N}_1[\psi](t, \boldsymbol{x}) = \kappa_1\psi(t, \boldsymbol{x}) + f_0(\psi(t, \boldsymbol{x})), \quad \boldsymbol{x} \in \Omega,\\
&f_0(\psi(t, \boldsymbol{x})) = M\left(1 - \psi(t, \boldsymbol{x})^2\right)\left(\psi(t, \boldsymbol{x}) + B(t, \boldsymbol{x})\right),\\
&B(t, \boldsymbol{x}) = 3(m(\sigma(t, \boldsymbol{x})) - m_{ref}u(t)), \quad -1 < B(t, \boldsymbol{x}) < 1,
\end{aligned} \tag{3.5}$$

and $\mathcal{I}$ is identity operator. We require that the stability constant κ_1 be selected as

$$\kappa_1 \geq \max_{|\xi|\leq 1} |f_0'(\xi)| = \max_{|\xi|\leq 1} M|-3\xi^2 - 2\xi B + 1| = 4M. \tag{3.6}$$

And for the nonlinear term f_0, there exists a $\beta \geq 1$, such that

$$f_0(\beta) = M\left(1 - \beta^2\right)(\beta + B) \leq 0 \leq f_0(-\beta) = M\left(1 - \beta^2\right)(-\beta + B). \tag{3.7}$$

Then we have the following lemma.

Lemma 3.1. *Under the requirement* (3.6)*, for any* $\xi \in [-\beta, \beta]$*, it holds that*

$$|\mathcal{N}_1[\xi]| \leq \kappa_1\beta.$$

In this study, we set $\beta = 1$. We are now in a position to show that problem (3.4) has a unique solution and preserves the maximum bound through the existing conclusions in [5]. The main MBP theorem can be stated as follows.

Theorem 3.1. *Given any constant* $T > 0$*, if* $|\psi_0(\boldsymbol{x})| \leq 1, \forall \boldsymbol{x} \in \Omega$*, then* (3.4) *with the initial condition and boundary condition* (3.3) *has a unique solution* $\psi \in C([0, T]; L^2)$ *and it satisfies* $\|\psi(t)\| \leq 1$ *for any* $t \in [0, T]$*.*

The proof is almost identical to the proof of Theorem 2.3 in [5], with the main modification being the substitution of the Dirichlet boundary condition. We omit here and leave it to the readers.

3.1.2. Fully Discrete Scheme

Next, we present the fully-discrete scheme. By discretizing the spatial component of equation (3.4) using the second-order central difference operator Δ_h to replace the Laplacian Δ, we obtain an ordinary differential equation (ODE) system :

$$\psi_t(t) + \mathcal{L}_{\kappa_1,h}\psi(t) = N_1(\psi, \sigma, u), \tag{3.8}$$

where

$$\begin{aligned}
&\mathcal{L}_{\kappa_1,h} = -\lambda\Delta_h + \kappa_1\mathcal{I},\\
&N_1(\psi, \sigma, u) = \kappa_1\psi + M\left(1 - \psi^2\right)\left(\psi + 3(m(\sigma) - m_{ref}u)\right).
\end{aligned} \tag{3.9}$$

For time discretization, we utilize the exponential time differencing (ETD) method. Given a time step size $\tau > 0$, we divide the time interval by $\{t_n = n\tau\}_{n\geq 0}$. Utilizing the constant variation formula, the solution of (3.4) within the interval $[t_n, t_{n+1}]$ satisfies:

$$\psi\left(t_{n+1}\right) = \mathrm{e}^{-\mathcal{L}_{\kappa_1,h}\tau}\psi\left(t_n\right) + \int_0^\tau e^{-\mathcal{L}_{\kappa_1,h}(\tau-s)}N_1(\psi(t_n + s), \sigma(t_n + s), u(t_n + s))ds. \tag{3.10}$$

The fully discrete first order ETD (ETD1) scheme comes from approximating $N_1(\psi(t_n+s),\sigma(t_n+s),u(t_n+s))$ by $N_1(\psi(t_n),\sigma(t_n),u(t_n))$. It takes the following form:

$$\psi^{n+1} = \mathrm{e}^{-\mathcal{L}_{\kappa_1,h}\tau}\psi^n + N_1(\psi^n,\sigma^n,u^n)\int_0^\tau e^{-\mathcal{L}_{\kappa_1,h}(\tau-s)}ds. \tag{3.11}$$

The fully discrete second order ETD Runge Kutta (ETDRK2) scheme comes from approximating $N_1(\psi(t_n+s),\sigma(t_n+s),u(t_n+s))$ by a linear interpolation based on $N_1(\psi(t_n),\sigma(t_n),u(t_n))$ and $N_1(\widetilde{\psi}(t_{n+1}),\widetilde{\sigma}(t_{n+1}),u(t_{n+1}))$. It takes the following form:

$$\begin{cases} \widetilde{\psi}^{n+1} = e^{-\mathcal{L}_{\kappa_1,h}\tau}\psi^n + N_1(\psi^n,\sigma^n,u^n)\displaystyle\int_0^\tau e^{-\mathcal{L}_{\kappa_1,h}(\tau-s)}ds, \\ \psi^{n+1} = e^{-\mathcal{L}_{\kappa_1,h}\tau}\psi^n + \displaystyle\int_0^\tau e^{-\mathcal{L}_{\kappa_1,h}(\tau-s)}\left(\left(1-\frac{s}{\tau}\right)N_1(\psi^n,\sigma^n,u^n) + \frac{s}{\tau}N_1(\widetilde{\psi}^{n+1},\widetilde{\sigma}^{n+1},u^n)\right)ds, \end{cases} \tag{3.12}$$

where $\widetilde{\psi}^{n+1}$ is an approximation of $\psi\left(t_{n+1}\right)$. σ^n and $\widetilde{\sigma}^{n+1}$ are described in Sec 3.2.1. Thus, the fully discrete first and second order ETD solutions for (2.3) can be derived by the relationships

$$\widetilde{\phi}^{n+1} = \frac{\widetilde{\psi}^{n+1}+1}{2}, \quad \phi^n = \frac{\psi^n+1}{2}. \tag{3.13}$$

3.1.3. Discrete MBPs

In order to prove the discrete MBP theorem, we need the following lemma.

Lemma 3.2 ([5])**.** *The Laplace operator Δ, enforced by the periodic boundary condition, Dirichlet boundary condition or homogeneous Neumann boundary condition, generates a contraction semigroup $\left\{e^{\Delta t}\right\}_{t\geq 0}$ with respect to the supremum norm on the subspace of $C(\bar{\Omega})$, and for any $\alpha\geq 0$, it holds that*

$$\left\|e^{t(\Delta-\alpha)}u\right\| \leq e^{-\alpha t}\|u\|, \quad t\geq 0,$$

for any $u\in C(\bar{\Omega})$ with $\bar{\Omega}=\Omega\cup\partial\Omega$.

It is evident from the literature [5] that the spatial discrete approximation Δ_h of Δ adheres to Lemma 3.2. Consequently, we can extend the discrete MBP-preserving outcomes to encompass fully discrete schemes.

Theorem 3.2. *(Discrete MBP of the ETD1/ETDRK2 schemes). If $|\psi_0|\leq 1$, κ_1 satisfies* (3.6)*, then the ETD1 scheme* (3.11) *and ETDRK2 scheme* (3.12) *preserve the discrete MBP unconditionally, i.e., for any time step size $\tau>0$, the ETD1 solution and ETDRK2 solution satisfie $\|\psi^n\|\leq 1$ for any $n\geq 0$.*

Proof. Since $|\psi_0|\leq 1$, it suffices to prove the theorem in the case that $\|\psi^n\|\leq 1$ and $\psi^n\not\equiv\pm 1$ deduce $\|\psi^{n+1}\|\leq 1$ for any n.

For the ETD1 scheme (3.11), according to Lemma 3.1, Lemma 3.2 and $\|\psi^n\|\leq 1$, it follows that

$$\begin{aligned} \left\|\psi^{n+1}\right\| &\leq \left\|e^{-\mathcal{L}_{\kappa_1,h}\tau}\right\|\|\psi^n\| + \int_0^\tau \left\|e^{-\mathcal{L}_{\kappa_1,h}(\tau-s)}\right\|\|N_1(\psi^n,\sigma^n,u^n)\|\,ds, \\ &\leq e^{-\kappa_1\tau} + \int_0^\tau e^{-\kappa_1(\tau-s)}\kappa_1 ds, \\ &= e^{-\kappa_1\tau} + \frac{1-e^{-\kappa_1\tau}}{\kappa_1}\kappa_1 = 1. \end{aligned} \tag{3.14}$$

For the ETDRK2 scheme (3.12), according to Lemma 3.1, Lemma 3.2 , $\|\psi^n\| \leq 1$, and $\left\|\widetilde{\psi}^{n+1}\right\| \leq 1$ (according to (3.14)), it follows that

$$\begin{aligned}
\left\|\psi^{n+1}\right\| &\leq \left\|e^{-\mathcal{L}_{\kappa_1,h}\tau}\right\| \|\psi^n\| \\
&\quad + \int_0^\tau \left\|e^{-\mathcal{L}_{\kappa_1,h}(\tau-s)}\right\| \left\|\left(1-\frac{s}{\tau}\right) N_1(\psi^n,\sigma^n,u^n) + \frac{s}{\tau} N_1(\widetilde{\psi}^{n+1},\widetilde{\sigma}^{n+1},u^n)\right\| ds, \\
&\leq e^{-\kappa_1\tau} + \int_0^\tau e^{-\kappa_1(\tau-s)} \left(\left(1-\frac{s}{\tau}\right)\kappa_1 + \frac{s}{\tau}\kappa_1\right) ds, \\
&= e^{-\kappa_1\tau} + \frac{1-e^{-\kappa_1\tau}}{\kappa_1}\kappa_1 = 1.
\end{aligned}$$

This proof is completed. □

Obviously, thanks to the relationships (3.13), it can easily be seen that if $\phi_0 \in [0,1]$ (or $|\psi_0| \leq 1$), then $\phi^n \in [0,1]$.

3.2. Critical nutrient σ

In this section, we will present non-negativity preserving schemes utilizing the ETD method for modeling nutrient dynamics.

3.2.1. Fully Discrete Scheme

To construct stable numerical schemes that preserve non-negativity for the critical nutrient concentration σ, we introduce a stabilizing constant $\kappa_2 > 0$ and rewrite equation (2.4) in an equivalent form:

$$\sigma_t(t,\boldsymbol{x}) + \mathcal{L}_{\kappa_2}\sigma(t,\boldsymbol{x}) = \mathcal{N}_2[\sigma](t,\boldsymbol{x}), \quad \text{in } Q_T, \tag{3.15}$$

where

$$\mathcal{L}_{\kappa_2} = -\eta\Delta + \gamma_h\mathcal{I} + \kappa_2\mathcal{I},$$

$$\mathcal{N}_2[\sigma](t,\boldsymbol{x}) = \kappa_2\sigma(t,\boldsymbol{x}) - (\gamma_c-\gamma_h)\,\sigma(t,\boldsymbol{x})\phi(t,\boldsymbol{x}) + S_h(1-\phi(t,\boldsymbol{x})) + (S_c - s(t))\,\phi(t,\boldsymbol{x}).$$

Here, $\mathcal{I}$ is identity operator, and ϕ is the unique solution of (2.3) satisfying $0 \leq \phi \leq 1$. With the initial and boundary conditions (2.9). We require that the stability constant κ_2 be selected as

$$\kappa_2 \geq (\gamma_c - \gamma_h)\,. \tag{3.16}$$

Let $\mathcal{L}_{\kappa_2,h} = -\eta\Delta_h + \gamma_h\mathcal{I} + \kappa_2\mathcal{I}$. Now we give the fully discrete ETD1 scheme

$$\sigma^{n+1} = \mathrm{e}^{-\mathcal{L}_{\kappa_2,h}\tau}\sigma^n + N_2(\phi^n,\sigma^n,s^n)\int_0^\tau e^{-\mathcal{L}_{\kappa_2,h}(\tau-s)}ds, \tag{3.17}$$

where

$$N_2(\phi^n,\sigma^n,s^n) = \kappa_2\sigma^n - (\gamma_c-\gamma_h)\,\sigma^n\phi^n + S_h(1-\phi^n) + (S_c - s^n)\,\phi^n.$$

And the fully-discrete ETDRK2 scheme is given by

$$\begin{cases}
\widetilde{\sigma}^{n+1} = e^{-\mathcal{L}_{\kappa_2,h}\tau}\sigma^n + N_2(\phi^n,\sigma^n,s^n)\displaystyle\int_0^\tau e^{-\mathcal{L}_{\kappa_2,h}(\tau-s)}ds, \\
\sigma^{n+1} = e^{-\mathcal{L}_{\kappa_2,h}\tau}\sigma^n + \displaystyle\int_0^\tau e^{-\mathcal{L}_{\kappa_2,h}(\tau-s)}\left(\left(1-\frac{s}{\tau}\right)N_2(\phi^n,\sigma^n,s^n) + \frac{s}{\tau}N_2(\widetilde{\phi}^{n+1},\widetilde{\sigma}^{n+1},s^n)\right)ds.
\end{cases} \tag{3.18}$$

Both ϕ^n and $\widetilde{\phi}^{n+1}$ have been mentioned in Sec 3.1.2.

3.2.2. Discrete Non-negativity

Next, we provide the following theorem to illustrate the non-negative preserving of the ETD schemes described above.

Theorem 3.3. *(Discrete non-negativity preserving of the ETD1/ETDRK2 schemes) If* $0 \leq \sigma_0 < \infty$, κ_2 *satisfies* (3.16), *then the ETD1 scheme* (3.17) *and the ETDRK2 scheme* (3.18) *preserve the non-negativity unconditionally, i.e., for any time step size* $\tau > 0$, *the ETD1 solution and the ETDRK2 solution satisfie* $0 \leq \sigma^n < \infty$.

Proof. Our aim is to show that if $0 \leq \sigma^n < \infty$, then it implies $0 \leq \sigma^{n+1} < \infty$. Based on the fact that $0 \leq \sigma^n < \infty$ and the properties of natural exponential functions, we observe that the first term and the integral in the second term on the right-hand side of equation (3.17) are both non-negative and bounded. Consequently, the theorem can be proven by establishing that $N_2(\phi^n, \sigma^n, s^n)$ is non-negative and bounded.

For the ETD1 scheme (3.17), by considering the condition (3.16), $s \leq S_c$, $\phi^n \in [0, 1]$ (as described in Section 3.1.3), and $0 \leq \sigma^n < \infty$, we can conclude that:

$$\begin{aligned} N_2(\phi^n, \sigma^n, s^n) &= \kappa_2 \sigma^n - (\gamma_c - \gamma_h)\, \sigma^n \phi^n + S_h(1 - \phi^n) + (S_c - s^n)\, \phi^n \\ &\geq (\gamma_c - \gamma_h)\, \sigma^n (1 - \phi^n) + S_h(1 - \phi^n) + (S_c - s^n)\, \phi^n \\ &\geq 0, \end{aligned} \tag{3.19}$$

that is, σ^{n+1} is non-negative and bounded.

For the ETDRK2 scheme (3.18), based on (3.19), we already know that $N_2(\phi^n, \sigma^n, s^n)$, $\widetilde{\sigma}^{n+1}$, and $N_2(\widetilde{\phi}^{n+1}, \widetilde{\sigma}^{n+1}, s^n)$ are non-negative and bounded. Similarly, by taking into account the conditions $0 \leq \sigma^n < \infty$, the properties of natural exponential functions, and $s \in [0, \tau]$, we can easily demonstrate that each term on the right-hand side of (3.18) is non-negative and bounded. Consequently, we can conclude that σ^{n+1} is both non-negative and bounded.

This is the complete proof. □

3.3. Tissue PSA p

In this section, we will present non-negativity preserving schemes based on the ETD method for modeling tissue PSA dynamics.

3.3.1. Fully Discrete Scheme

By following the same procedure as in Section 3.2.1, we can rewrite equation (2.5) in an equivalent form:

$$p_t(t, \boldsymbol{x}) + \mathcal{L}_3 p(t, \boldsymbol{x}) = \mathcal{N}_3[\phi](t, \boldsymbol{x}), \quad \text{in } Q_T, \tag{3.20}$$

where

$$\mathcal{L}_3 = -D\Delta + \gamma_p \mathcal{I},$$
$$\mathcal{N}_3[\phi](t, \boldsymbol{x}) = \alpha_h(1 - \phi(t, \boldsymbol{x})) + \alpha_c \phi(t, \boldsymbol{x}).$$

Here, $\mathcal{I}$ is identity operator, and ϕ is the unique solution of (2.3) satisfying $0 \leq \phi \leq 1$. With the initial and boundary conditions (2.9).

Let $\mathcal{L}_{3,h} = -D\Delta_h + \gamma_p \mathcal{I}$. Now we give the fully discrete ETD1 scheme as follows

$$p^{n+1} = \mathrm{e}^{-\mathcal{L}_{3,h}\tau} p^n + N_3(\phi^n) \int_0^\tau e^{-\mathcal{L}_{3,h}(\tau - s)} ds, \tag{3.21}$$

where

$$N_3(\phi^n) = \alpha_h(1-\phi^n) + \alpha_c\phi^n.$$

And the fully-discrete ETDRK2 scheme is given by

$$\begin{cases} \widetilde{p}^{n+1} = e^{-\mathcal{L}_{3,h}\tau}p^n + N_3(\phi^n)\displaystyle\int_0^\tau e^{-\mathcal{L}_{3,h}(\tau-s)}ds, \\ p^{n+1} = e^{-\mathcal{L}_{3,h}\tau}p^n + \displaystyle\int_0^\tau e^{-\mathcal{L}_{3,h}(\tau-s)}\left(\left(1-\frac{s}{\tau}\right)N_3(\phi^n) + \frac{s}{\tau}N_3(\widetilde{\phi}^{n+1})\right)ds, \end{cases} \tag{3.22}$$

Both ϕ^n and $\widetilde{\phi}^{n+1}$ have been mentioned in Sec 3.1.2.

3.3.2. Discrete Non-negativity

We have derived fully-discrete ETD schemes for the computation of tissue PSA concentration, and now we will demonstrate the unconditional preservation of non-negativity in these schemes through the following theorem.

Theorem 3.4. *(Discrete non-negativity preserving of the ETD1/ETDRK2 scheme) If $0 \le p_0 < \infty$, then the ETD1 scheme* (3.21) *and the ETDRK2 scheme* (3.22) *preserve the non-negativity unconditionally, i.e., for any time step size $\tau > 0$, the ETD1 solution and the ETDRK2 solution satisfie $0 \le p^n < \infty$.*

Proof. The proof can be carried out similarly to the previous section by demonstrating that $0 \le p^n < \infty$ implies $0 \le p^{n+1} < \infty$.

For the ETD 1 scheme (3.21), from the conditions $0 \le p^n < \infty$ and the properties of natural exponential functions, it can be observed that the first term and the integral in the second term on the right-hand side of equation (3.21) are both non-negative and bounded. Furthermore, since $\phi^n \in [0,1]$ (as described in Section 3.1.3) and α_h, α_c are positive constants, it can be concluded that:

$$N_3(\phi^n) = \alpha_h(1-\phi^n) + \alpha_c\phi^n \ge 0, \tag{3.23}$$

that is, p^{n+1} is non-negative and bounded.

For the ETDRK2 scheme (3.22), we can refer to (3.23) to ascertain the non-negativity and boundedness of $N_3(\phi^n)$, $\widetilde{p}^{n+1}$, and $N_3(\widetilde{\phi}^{n+1})$. Given the condition $0 \le p^n < \infty$, the properties of natural exponential functions, and the range $s \in [0,\tau]$, it becomes evident that each term on the right-hand side of (3.22) is non-negative and bounded. Consequently, we can conclude that p^{n+1} is both non-negative and bounded.

This is the complete proof. □

3.4. Fast implementation of the ETD schemes

In order to ensure efficient computation when employing ETD schemes, it becomes essential to utilize fast algorithms that can effectively calculate the product between the matrices and the functions $\{\Phi_n\}_{n=0,1,2}(\mathcal{L}\tau)$. In this section, we utilize the FFT-based fast implementation of the ETD schemes [4, 17] to solve the system with a Dirichlet boundary condition for ψ, as well as Neumann boundary conditions for σ and p.

Define the $\{\Phi_i\}_{i=0,1,2}$ functions

$$\Phi_0(L) := \mathrm{e}^{-L}, \quad \Phi_1(L) := \frac{1-\mathrm{e}^{-L}}{L}, \quad \Phi_2(L) := \frac{\mathrm{e}^{-L}-1+L}{L^2}, \quad L \ne 0. \tag{3.24}$$

We can write the coupled systems as the following equivalent schemes:

(ETD1 scheme)

$$\begin{cases} \psi^{n+1} = \Phi_0\left(\mathcal{L}_{\kappa_1,h}\tau\right)\psi^n + \tau\Phi_1\left(\mathcal{L}_{\kappa_1,h}\tau\right)N_1(\psi^n,\sigma^n,u^n), \\ \phi^{n+1} = (\psi^{n+1}+1)/2, \\ \sigma^{n+1} = \Phi_0\left(\mathcal{L}_{\kappa_2,h}\tau\right)\sigma^n + \tau\Phi_1\left(\mathcal{L}_{\kappa_2,h}\tau\right)N_2(\phi^n,\sigma^n,s^n), \\ p^{n+1} = \Phi_0\left(\mathcal{L}_{3,h}\tau\right)p^n + \tau\Phi_1\left(\mathcal{L}_{3,h}\tau\right)N_3(\phi^n). \end{cases} \tag{3.25}$$

(ETDRK2 scheme)

$$\begin{cases} \widetilde{\psi}^{n+1} = \Phi_0\left(\mathcal{L}_{\kappa_1,h}\tau\right)\psi^n + \tau\Phi_1\left(\mathcal{L}_{\kappa_1,h}\tau\right)N_1(\psi^n,\sigma^n,u^n), \\ \widetilde{\phi}^{n+1} = (\widetilde{\psi}^{n+1}+1)/2, \\ \widetilde{\sigma}^{n+1} = \Phi_0\left(\mathcal{L}_{\kappa_2,h}\tau\right)\sigma^n + \tau\Phi_1\left(\mathcal{L}_{\kappa_2,h}\tau\right)N_2(\phi^n,\sigma^n,s^n), \\ \widetilde{p}^{n+1} = \Phi_0\left(\mathcal{L}_{3,h}\tau\right)p^n + \tau\Phi_1\left(\mathcal{L}_{3,h}\tau\right)N_3(\phi^n), \\ \psi^{n+1} = \widetilde{\psi}^{n+1} + \tau\Phi_2\left(\mathcal{L}_{\kappa_1,h}\tau\right)\left(N_1(\widetilde{\psi}^{n+1},\widetilde{\sigma}^{n+1},u^n) - N_1(\psi^n,\sigma^n,u^n)\right), \\ \phi^{n+1} = (\psi^{n+1}+1)/2, \\ \sigma^{n+1} = \widetilde{\sigma}^{n+1} + \tau\Phi_2\left(\mathcal{L}_{\kappa_2,h}\tau\right)\left(N_2(\widetilde{\phi}^{n+1},\widetilde{\sigma}^{n+1},s^n) - N_2(\phi^n,\sigma^n,s^n)\right), \\ p^{n+1} = \widetilde{p}^{n+1} + \tau\Phi_2\left(\mathcal{L}_{3,h}\tau\right)\left(N_3(\widetilde{\phi}^{n+1}) - N_3(\phi^n)\right). \end{cases} \tag{3.26}$$

To discretize the spatial domain, we employ the second-order central difference method. Consider a rectangular domain Ω defined by $0 \le x \le L_d$ and $0 \le y \le L_d$. We utilize a uniform mesh in both directions, such that $(x_i, y_j) = (ih_x, jh_y)$ for $0 \le i \le N_x$ and $0 \le j \le N_y$, where $h_x = L_d/N_x$ and $h_y = L_d/N_y$. The numerical solutions are denoted as $\psi_{i,j}(t) \approx \psi(t, x_i, y_j)$, $\sigma_{i,j}(t) \approx \sigma(t, x_i, y_j)$, and $p_{i,j}(t) \approx p(t, x_i, y_j)$ for $0 \le i \le N_x$ and $0 \le j \le N_y$. We set the equidistant time step in the discrete-time system as $\tau = T/N_t$, with $t_n = n\tau$ for $n = 0, \ldots, N_t$.

Let us assume $N_x = N_y = N$, resulting in $h_x = h_y = h$. The discretized Laplacian can be expressed as follows:

$$(-\Delta_h\psi)_{i,j} = \frac{1}{h^2}\left[4\psi_{i,j} - \psi_{i+1,j} - \psi_{i-1,j} - \psi_{i,j+1} - \psi_{i,j-1}\right],$$

and the same expression holds for $(-\Delta_h\sigma)_{i,j}$ and $(-\Delta_h p)_{i,j}$. The operator $\mathcal{L}_{\kappa_1,h}$ arises from Δ_h with the Dirichlet condition, while $\mathcal{L}_{\kappa 2,h}$ and $\mathcal{L}_{3,h}$ arise from Δ_h with Neumann boundary conditions. Denote by $\mathcal{S}$ and $\mathcal{C}$ the 2D DST (discrete sine transform, type I) and DCT (discrete cosine transform, type I) operators, respectively. Then, for any $V = (V_{k,l}) \in \mathbb{C}^{N\times N}$, the action of the operators

$$\Lambda_1 := \mathcal{S}\mathcal{L}_{\kappa_1,h}\mathcal{S}^{-1}, \quad \Lambda_2 := \mathcal{C}\mathcal{L}_{\kappa_2,h}\mathcal{C}^{-1}, \quad \Lambda_3 := \mathcal{C}\mathcal{L}_{3,h}\mathcal{C}^{-1},$$

can be implemented using the following expressions:

$$(\Lambda_1 V)_{k,l} = \lambda_{1,k,l}V_{k,l}, \quad (\Lambda_2 V)_{k,l} = \lambda_{2,k,l}V_{k,l}, \quad (\Lambda_3 V)_{k,l} = \lambda_{3,k,l}V_{k,l}, \quad 1 \le k,l \le N,$$

where $\lambda_{1,k,l}$, $\lambda_{2,k,l}$ and $\lambda_{3,k,l}$ denote the eigenvalues of the operators $\mathcal{L}_{\kappa_1,h}$, $\mathcal{L}_{\kappa_2,h}$ and $\mathcal{L}_{3,h}$

respectively. These eigenvalues can be computed as follows:

$$\lambda_{1,k,l} = \kappa_1 - \frac{4\lambda}{h^2}\sin^2\left(\frac{k\pi}{2N}\right) - \frac{4\lambda}{h^2}\sin^2\left(\frac{l\pi}{2N}\right), \quad k,l = 1,2,\ldots,N-1,$$
$$\lambda_{2,k,l} = \kappa_2 + \gamma_h - \frac{4\eta}{h^2}\sin^2\left(\frac{(k-1)\pi}{2N}\right) - \frac{4\eta}{h^2}\sin^2\left(\frac{(l-1)\pi}{2N}\right), \quad k,l = 1,2,\ldots,N+1,$$
$$\lambda_{3,k,l} = \gamma_p - \frac{4D}{h^2}\sin^2\left(\frac{(k-1)\pi}{2N}\right) - \frac{4D}{h^2}\sin^2\left(\frac{(l-1)\pi}{2N}\right), \quad k,l = 1,2,\ldots,N+1.$$

According to Lemma 2.2 (4) of [4], for $\gamma = 0, 1, 2$, we have

$$\Phi_\gamma\left(\mathcal{L}_{\kappa_1,h}\tau\right) = \mathcal{S}^{-1}\Phi_\gamma\left(\Lambda_1\tau\right)\mathcal{S}, \quad \left(\Phi_\gamma\left(\Lambda_1\tau\right)V\right)_{k,l} = \Phi_\gamma\left(\lambda_{1,k,l}\tau\right)V_{k,l}, \quad k,l = 1,2,\ldots,N-1,$$
$$\Phi_\gamma\left(\mathcal{L}_{\kappa_2,h}\tau\right) = \mathcal{C}^{-1}\Phi_\gamma\left(\Lambda_2\tau\right)\mathcal{C}, \quad \left(\Phi_\gamma\left(\Lambda_2\tau\right)V\right)_{k,l} = \Phi_\gamma\left(\lambda_{2,k,l}\tau\right)V_{k,l}, \quad k,l = 1,2,\ldots,N+1,$$
$$\Phi_\gamma\left(\mathcal{L}_{3,h}\tau\right) = \mathcal{C}^{-1}\Phi_\gamma\left(\Lambda_3\tau\right)\mathcal{C}, \quad \left(\Phi_\gamma\left(\Lambda_3\tau\right)V\right)_{k,l} = \Phi_\gamma\left(\lambda_{3,k,l}\tau\right)V_{k,l}, \quad k,l = 1,2,\ldots,N+1.$$

Remark 3.1. *Our methodology involves utilizing the fast Fourier transform (FFT) to compute the discrete cosine transform (DCT) and discrete sine transform (DST) through the following steps.*

As an illustration, let us focus on the x-direction, similar to the y-direction. For DST, we begin by considering any vector of length $\mathrm{N_x}-1$*, denoted by* $\psi = [\psi_1, \psi_2, \ldots, \psi_{N_x-1}]^T$*. We then define its reflection vector of length* $\mathrm{N_x}-1$ *as* $\hat{\psi} = [\psi_{N_x-1}, \psi_{N_x-2}, \ldots, \psi_1]^T$*. Next, we apply the* $2N_x$ *FFT to the vector* $v_1 = \left[0, \psi, 0, -\hat{\psi}\right]^T$*, and subsequently extract the second to* $\mathrm{N_x}$*-th components of* v_1 *and divide them by* $-2i$*.*

Similarly, for DCT, we start by considering any vector of length $\mathrm{N_x}+1$*, denoted by* $\sigma = [\sigma_1, \sigma_2, \ldots, \sigma_{N_x+1}]^T$*. We then define its reflection vector of length* $\mathrm{N_x}-1$ *as* $\hat{\sigma} = [\sigma_{N_x-1}, \sigma_{N_x-2}, \ldots, \sigma_2]^T$*. Next, we apply the* $2N_x$ *FFT to the vector* $v_2 = [\sigma, \hat{\sigma}]^T$*, and subsequently extract the first* $\mathrm{N_x}+1$ *components of* v_2 *and divide them by 2. For further details, please refer to section 4.4 of [35].*

Remark 3.2. *Note that for* ψ^n *with non-homogeneous Dirichlet boundary condition, we need to define a* $\mathbf{w} = \psi_{x1} + \psi_{y1}$ *and add the boundary conditions to nonlinear term* N_1*, where*

$$\psi_{x1} = \frac{\lambda}{h_x^2}\begin{pmatrix} -1 & -1 & \cdots & -1 \\ 0 & 0 & \cdots & 0 \\ \vdots & \vdots & \ddots & \vdots \\ 0 & 0 & \cdots & 0 \\ -1 & -1 & \cdots & -1 \end{pmatrix}_{(N_x-1)\times(N_y-1)} \tag{3.27}$$

$$\psi_{y1} = \frac{\lambda}{h_y^2}\begin{pmatrix} -1 & 0 & \cdots & 0 & -1 \\ -1 & 0 & \cdots & 0 & -1 \\ \vdots & \vdots & \vdots & \ddots & \vdots \\ -1 & 0 & \cdots & 0 & -1 \end{pmatrix}_{(N_x-1)\times(N_y-1)} \tag{3.28}$$

Furthermore, it is important to emphasize that the resulting dimensions of ψ^n *are* $(N_x-1)\times(N_y-1)$*, while the dimensions of* σ^n *and* p^n *with Neumann boundary conditions are* $(N_x+1)\times(N_y+1)$*. Consequently, once* $\psi^n_{(N_x-1)\times(N_y-1)}$ *has been computed, we can obtain updated values of* $\phi^n_{(N_x+1)\times(N_y+1)}$ *using equation* (3.13) *and incorporate the Dirichlet boundary conditions. This, in turn, enables us to calculate updated values of* $\sigma^n_{(N_x+1)\times(N_y+1)}$ *and* $p^n_{(N_x+1)\times(N_y+1)}$*.*

4. Simulations

This section presents simulations utilizing the model and algorithm outlined earlier, employing the parameter values specified in Table 1 as described in [3]. The simulations are divided into two parts: tumor growth simulations without treatment, and tumor growth simulations with treatment. In the first part, we examine two scenarios: mild tumors and aggressive tumors. In the second part, three distinct drug treatment plans are explored.

We consider the 2D square domain with a side length of $L_d = 3,000\mu m$ and let $N_x = N_y = N = 2048$ and time step is chosen by $\Delta t = 0.03$, and the final time T=365 days. According to [3], the initial condition for the tumor phase field ϕ is approximated as follows:

$$\phi_0(x,y) = 0.5 - 0.5\tanh\left(10\left(\sqrt{\frac{(x-L_d/2)^2}{a^2} + \frac{(y-L_d/2)^2}{b^2}} - 1\right)\right),$$

where $a = 150\mu$m and $b = 200\mu$m. The initial conditions for the nutrient and the tissue PSA are approximations as

$$\sigma_0 = c_\sigma^0 + c_\sigma^1\phi_0, \quad p_0 = c_p^0 + c_p^1\phi_0,$$

where $c_\sigma^0 = 1$ g/L, $c_\sigma^1 = -0.8$ g/L, $c_p^0 = 0.0625$ng/mL/cc, and $c_p^1 = 0.7975$ng/mL/cc.

4.1. Simulation of PCa growth without treatment

In the subsequent simulations, we investigate the growth of untreated tumors by setting the functions $u(t)$ and $s(t)$, which represent the effects of drugs, to zero. We consider two scenarios of PCa: a mild tumor and an aggressive tumor. To achieve this, we adjust the proliferation index ρ and apoptosis index A in the function $m(\sigma)$ as presented in equation (2.1). Specifically, mild tumors are characterized by lower values of $|\rho| - |A|$ (with $\rho = 8/15$ and $A = -1/3$), while more aggressive tumors require higher values of $|\rho| - |A|$ (with $\rho = 1$ and $A = -137/210$).

To investigate the impact of varying nutrient supply and consumption by tumor tissue on tumor growth, we simulate the following five cases by selecting different values for the nutrient supply parameter S_c and the nutrient uptake parameter γ_c by tumor tissue: (a) baseline, with $S_c = 2.75$ and $\gamma_c = 17$; (b) higher nutrient supply, with $S_c = 3.125$ and $\gamma_c = 17$; (c) lower nutrient supply, with $S_c = 2.375$ and $\gamma_c = 17$; (d) higher tumor metabolism, with $S_c = 2.75$ and $\gamma_c = 18$; (e) lower tumor metabolism, with $S_c = 2.75$ and $\gamma_c = 16$.

Figures 1-5 depict simulations of mild tumor growth, along with the diffusion of nutrients and tissue PSA under cases (a)-(e). Figure 6 presents the serum PSA levels and tumor volume of mild tumors, demonstrating a similar trend in changes between tumor volume and serum PSA levels. The simulation results indicate that mild tumors maintain a spherical shape throughout their growth, consistent with previous studies in [3, 9]. Moreover, mild tumors tend to exhibit faster growth and reach larger sizes under conditions of (b) higher nutrient supply and (e) lower tumor metabolism. While their growth rates gradually decelerate over time, mild tumors eventually disappear under conditions of (c) lower nutrient supply and (d) higher tumor metabolism.

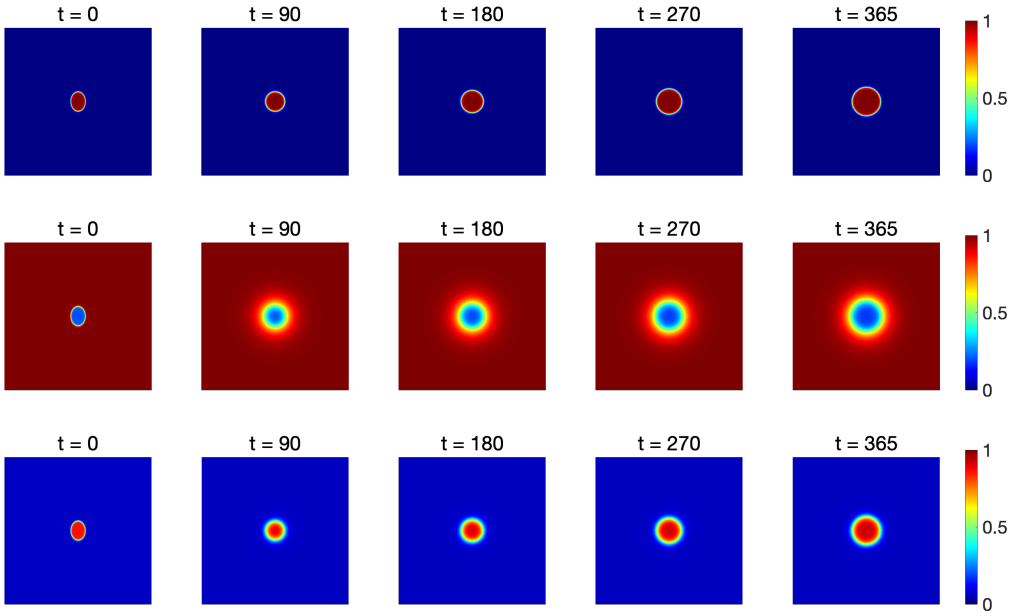

Figure 1: Tumor growth (the first row), Nutrient distribution (the second row) and PSA distribution (the third row) of mild tumors without treatment under (a) baseline, with $S_c = 2.75$ and $\gamma_c = 17$.

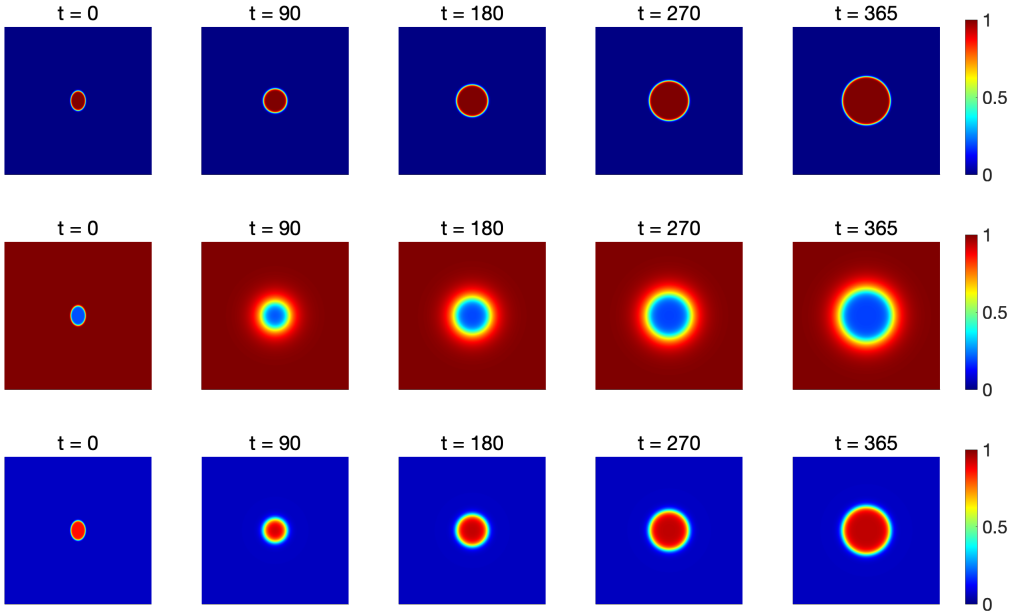

Figure 2: Tumor growth (the first row), Nutrient distribution (the second row) and PSA distribution (the third row) of mild tumors without treatment under (b) higher nutrient supply, with $S_c = 3.125$ and $\gamma_c = 17$.

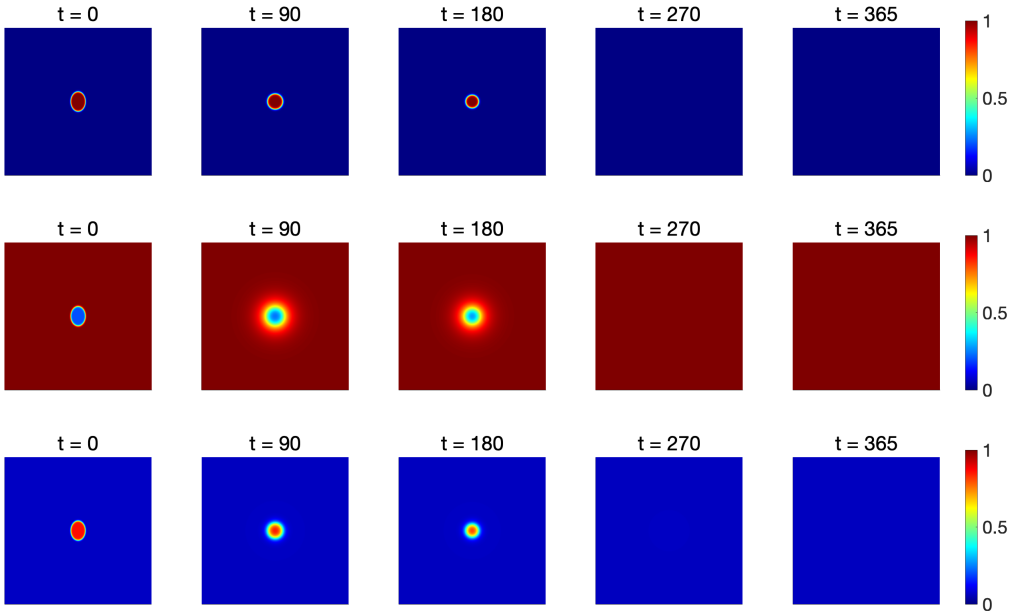

Figure 3: Tumor growth (the first row), Nutrient distribution (the second row) and PSA distribution (the third row) of mild tumors without treatment under (c) lower nutrient supply, with $S_c = 2.375$ and $\gamma_c = 17$.

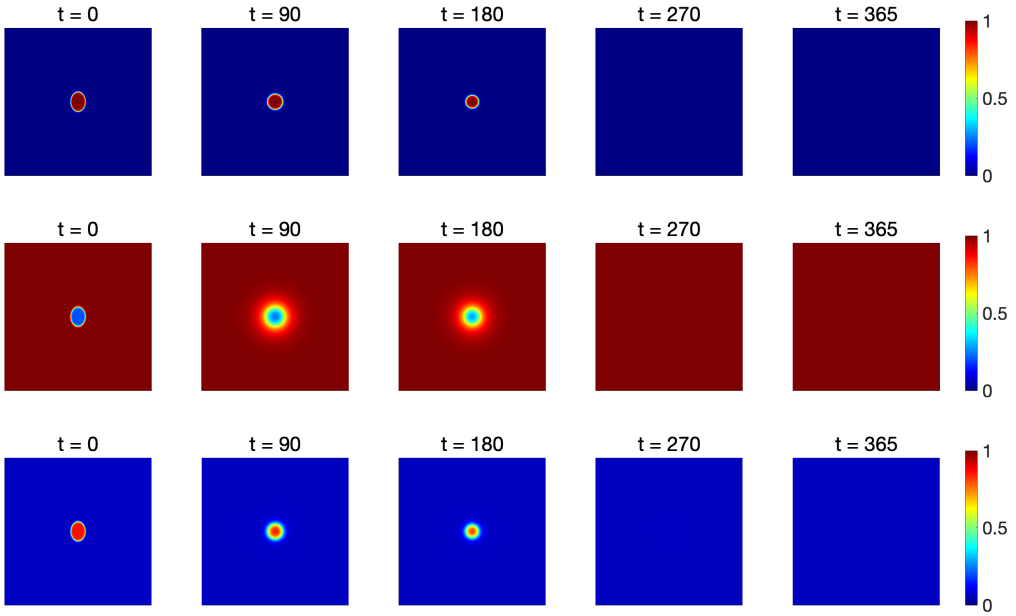

Figure 4: Tumor growth (the first row), Nutrient distribution (the second row) and PSA distribution (the third row) of mild tumors without treatment under (d) higher tumor metabolism, with $S_c = 2.75$ and $\gamma_c = 18$.

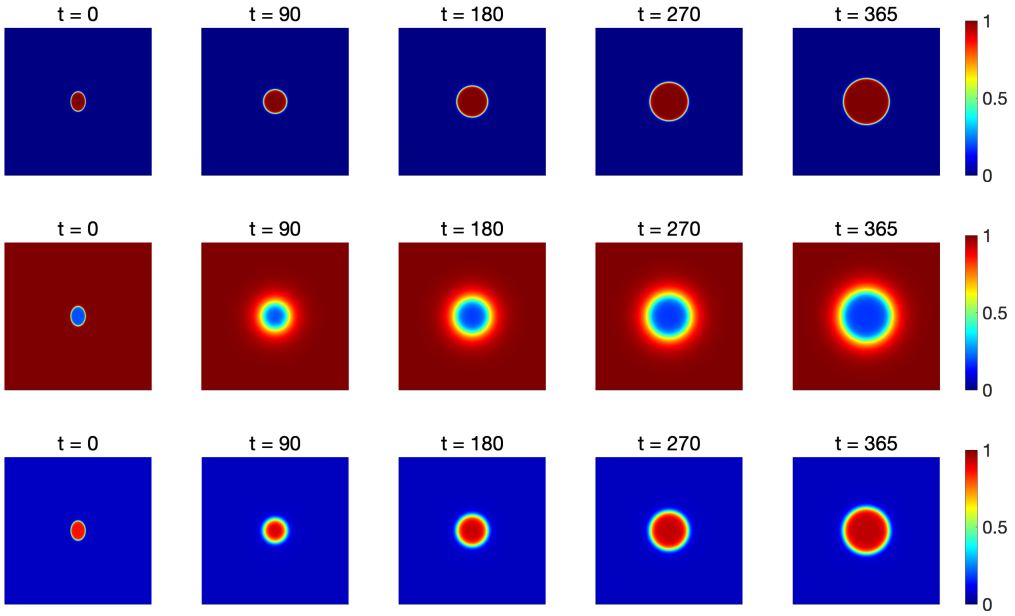

Figure 5: Tumor growth (the first row), Nutrient distribution (the second row) and PSA distribution (the third row) of mild tumors without treatment under (e) lower tumor metabolism, with $S_c = 2.75$ and $\gamma_c = 16$.

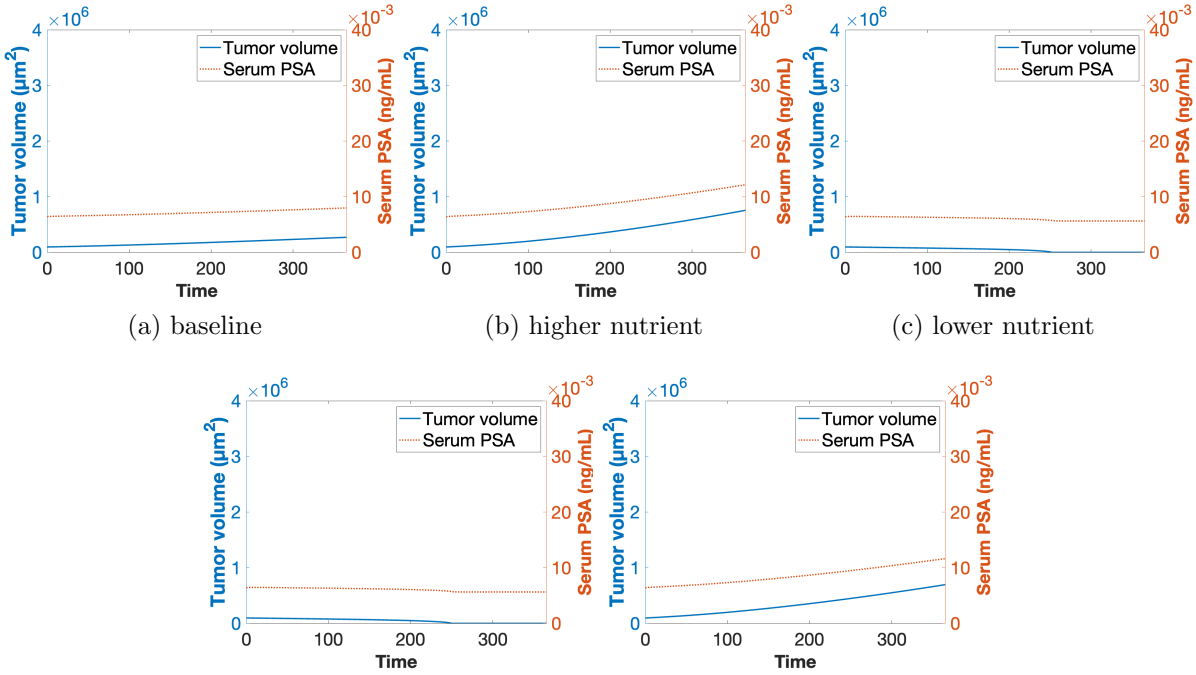

(a) baseline (b) higher nutrient (c) lower nutrient

(d) higher metabolism (e) lower metabolism

Figure 6: Tumor volume and serum PSA of mild tumors without treatment

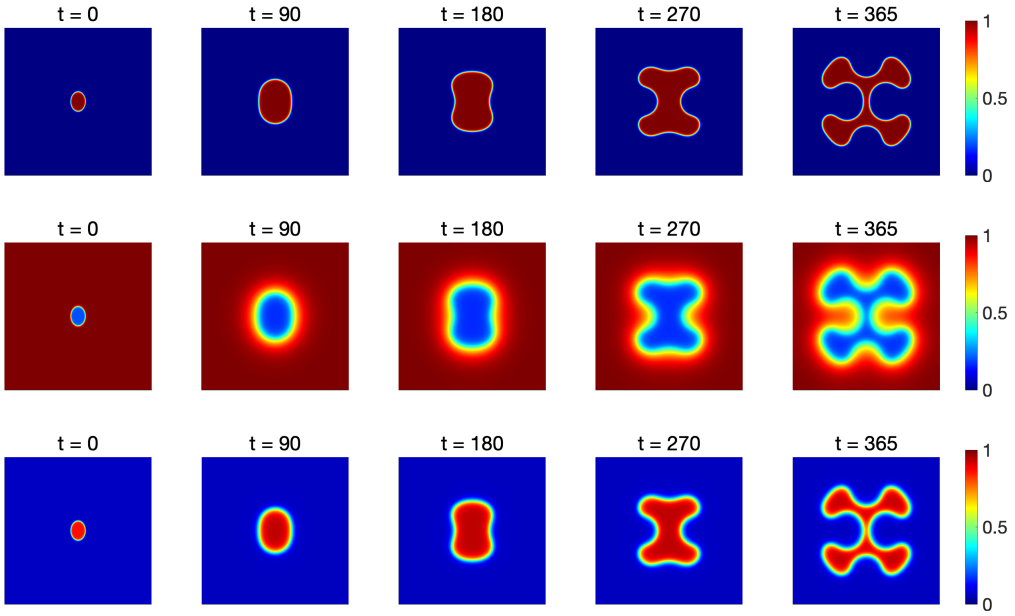

Figure 7: Tumor growth (the first row), Nutrient distribution (the second row) and PSA distribution (the third row) of aggressive tumors without treatment under (a) baseline, with $S_c = 2.75$ and $\gamma_c = 17$.

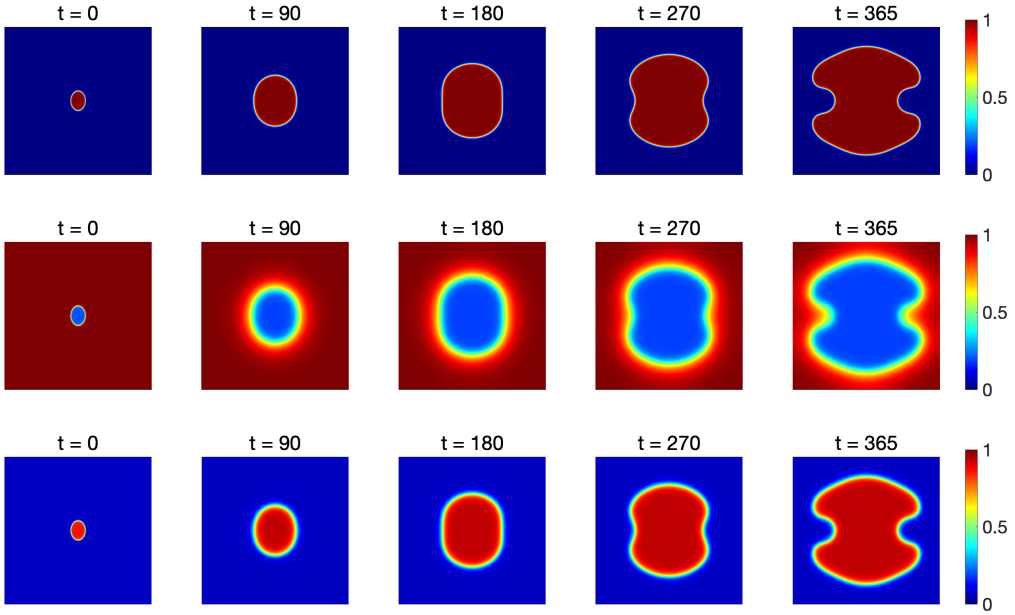

Figure 8: Tumor growth (the first row), Nutrient distribution (the second row) and PSA distribution (the third row) of aggressive tumors without treatment under (b) higher nutrient supply, with $S_c = 3.125$ and $\gamma_c = 17$.

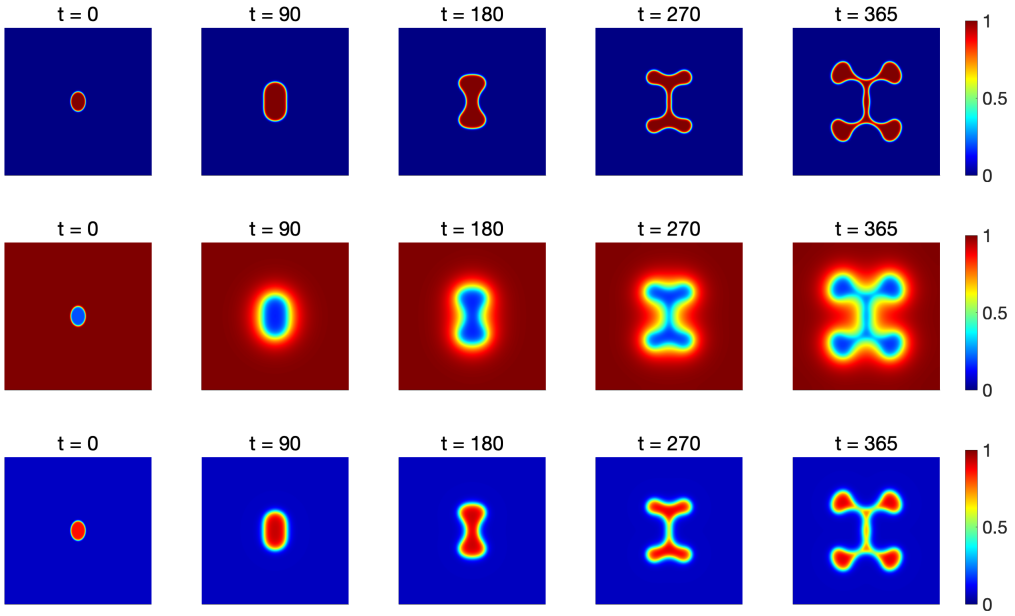

Figure 9: Tumor growth (the first row), Nutrient distribution (the second row) and PSA distribution (the third row) of aggressive tumors without treatment under (c) lower nutrient supply, with $S_c = 2.375$ and $\gamma_c = 17$.

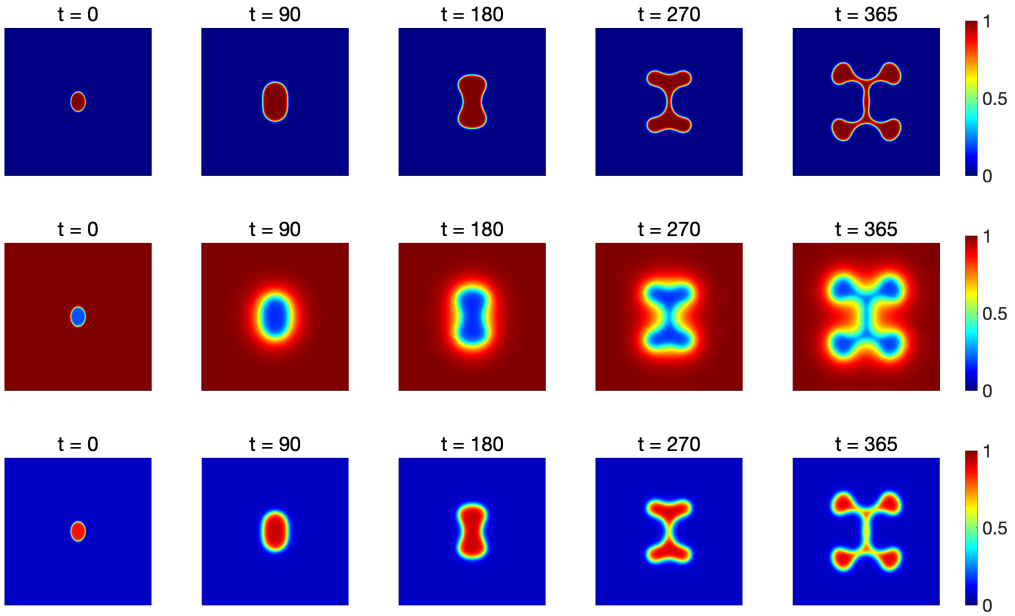

Figure 10: Tumor growth (the first row), Nutrient distribution (the second row) and PSA distribution (the third row) of aggressive tumors without treatment under (d) higher tumor metabolism, with $S_c = 2.75$ and $\gamma_c = 18$.

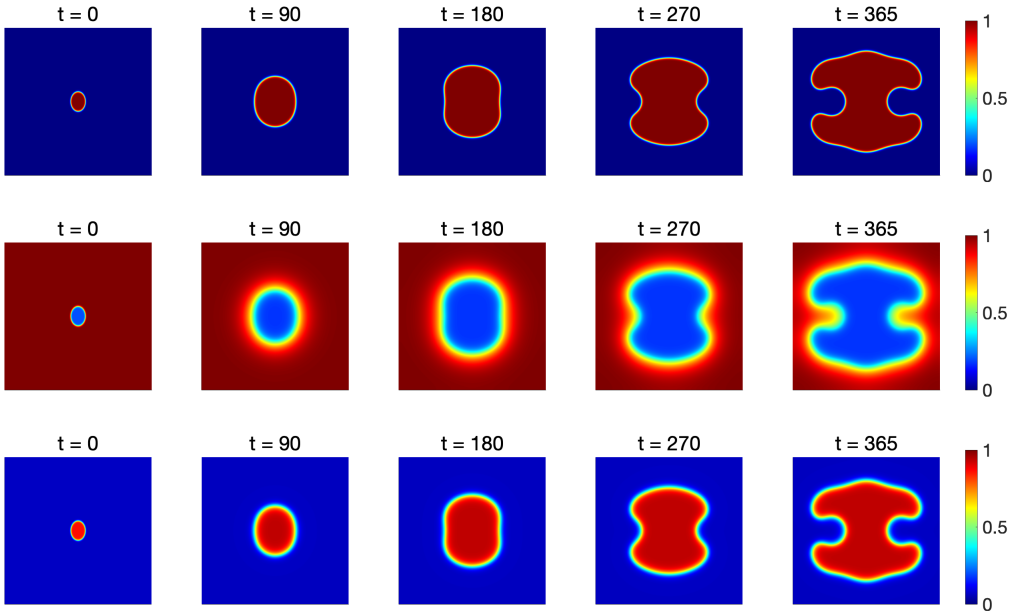

Figure 11: Tumor growth (the first row), Nutrient distribution (the second row) and PSA distribution (the third row) of aggressive tumors without treatment under (e) lower tumor metabolism, with $S_c = 2.75$ and $\gamma_c = 16$.

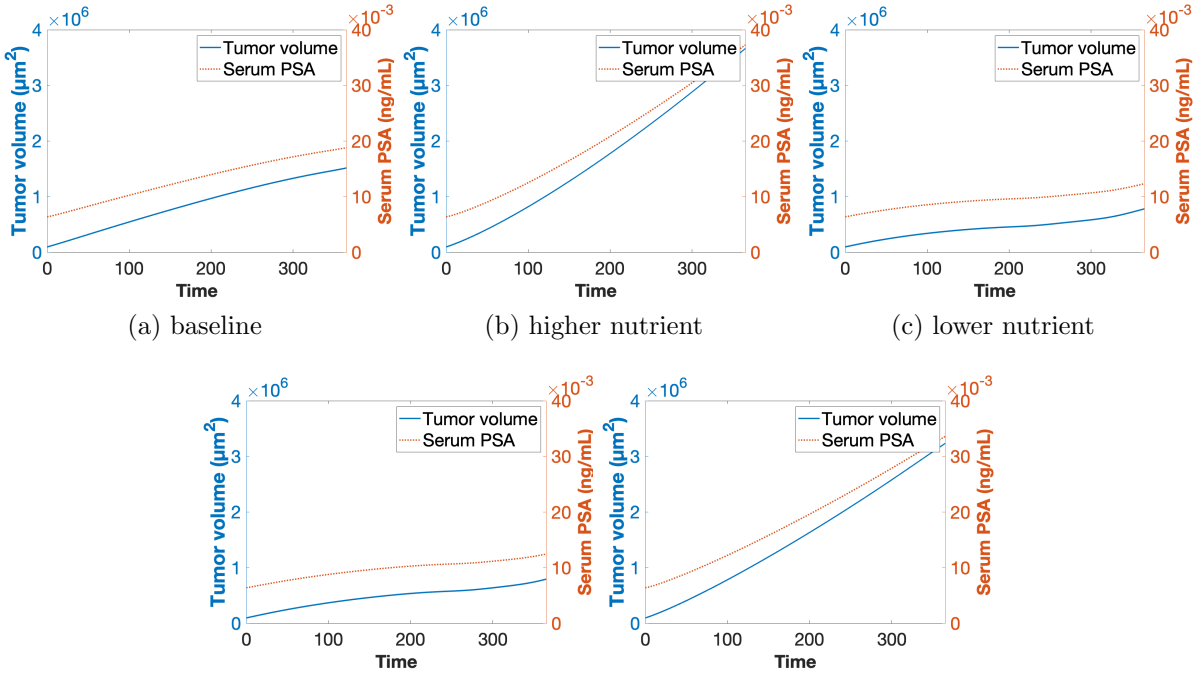

(a) baseline (b) higher nutrient (c) lower nutrient

(d) higher metabolism (e) lower metabolism

Figure 12: Tumor volume and serum PSA of aggressive tumors without treatment

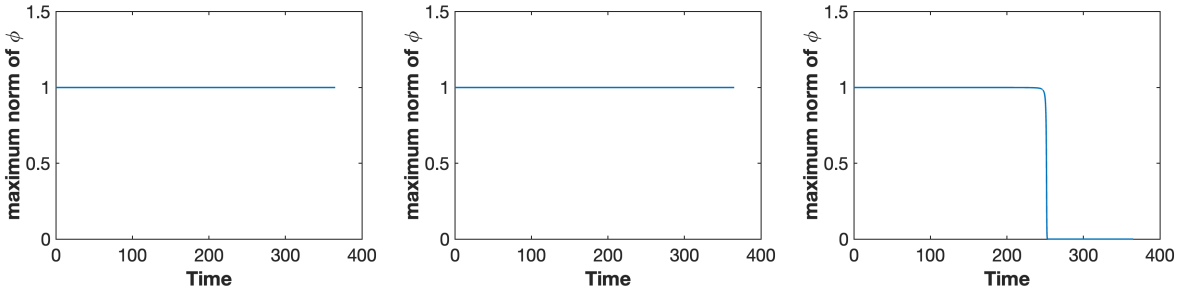

(a) baseline (b) higher nutrient (c) lower nutrient

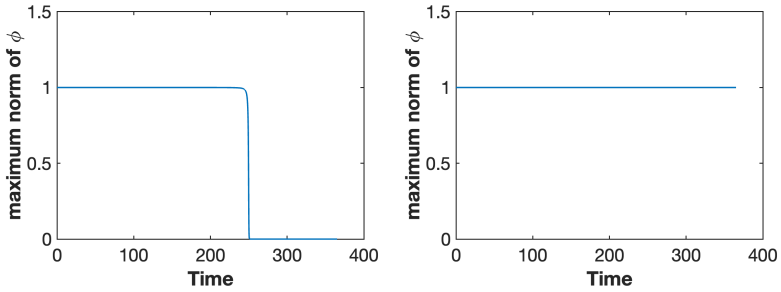

(d) higher metabolism (e) lower metabolism

Figure 13: MBP test of mild tumors without treatment

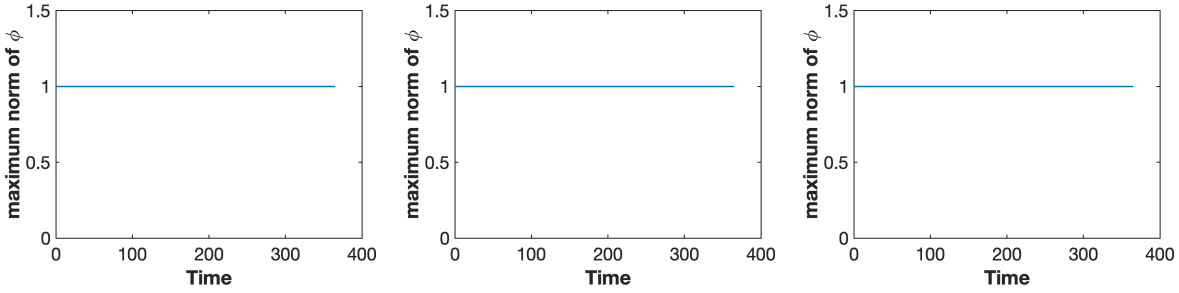

(a) baseline (b) higher nutrient (c) lower nutrient

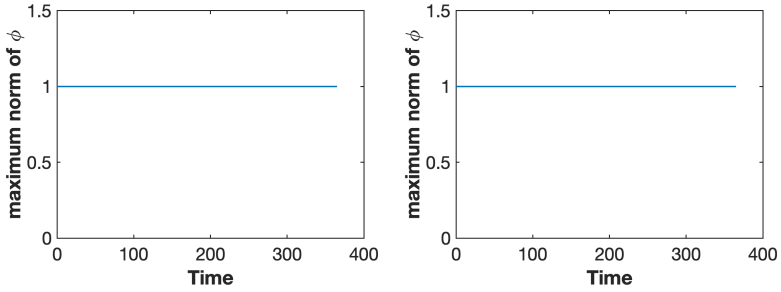

(d) higher metabolism (e) lower metabolism

Figure 14: MBP test of aggressive tumors without treatment

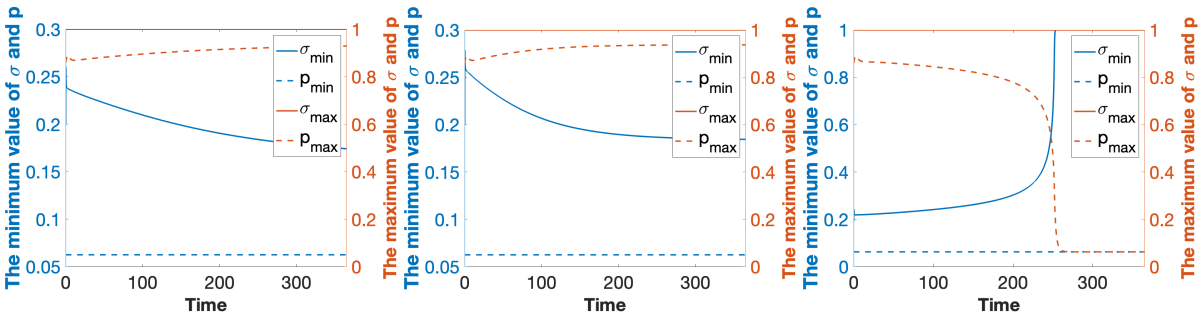

(a) baseline (b) higher nutrient (c) lower nutrient

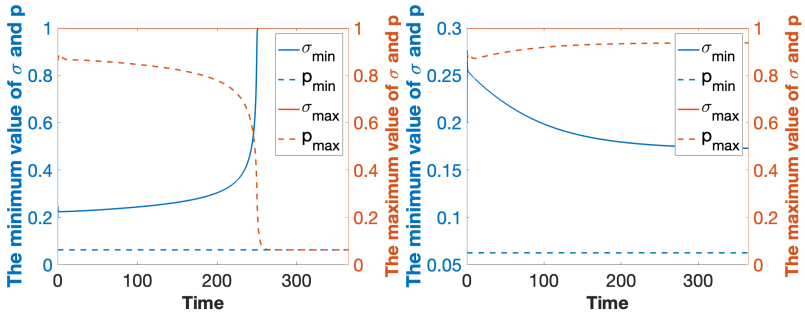

(d) higher metabolism (e) lower metabolism

Figure 15: Non-negative and bounded test of mild tumors without treatment

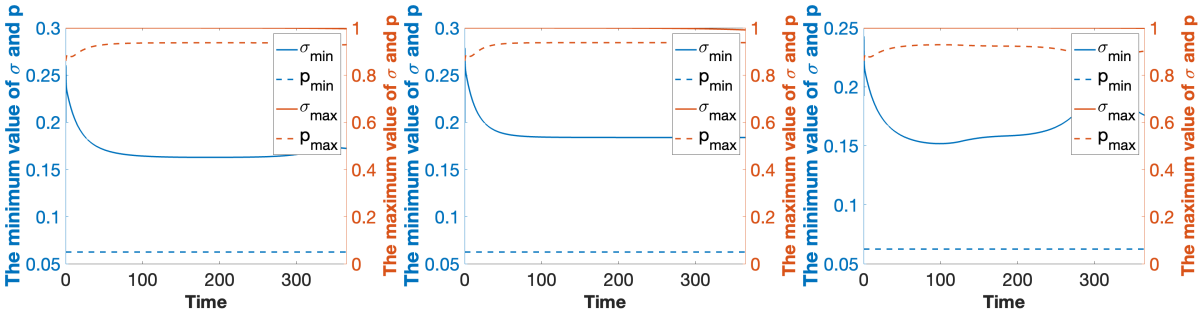

(a) baseline (b) higher nutrient (c) lower nutrient

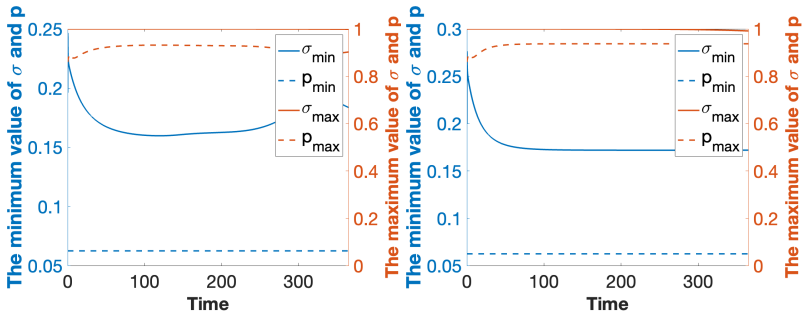

(d) higher metabolism (e) lower metabolism

Figure 16: Non-negative and bounded test of aggressive tumors without treatment

Figures 7-11 depict simulations of aggressive tumor growth, along with nutrient and PSA diffusion patterns, under five distinct scenarios (a)-(e). Additionally, in Figure 12, the serum PSA levels and tumor volume are presented, revealing a consistent trend in

their changes, which aligns with the previous research [3, 36]. While aggressive tumors initially exhibit spherical growth patterns similar to mild tumors, they undergo a shape transformation in later stages, developing finger-like structures. This phenomenon aligns with observations made in previous studies [9]. Specifically, under conditions of (b) higher nutrient supply and (e) lower tumor metabolism, aggressive tumors demonstrate rapid shape transformation, with their branching structures becoming progressively thinner over time. Conversely, under conditions of (c) lower nutrient supply and (d) higher tumor metabolism, the shape transformation of aggressive tumors decelerates, resulting in thicker branching structures observed only in the later stages of growth.

In Figures 13-14, we assess the evolution of the maximum norms of ϕ for mild and aggressive tumors, respectively. Furthermore, Figures 15-16 examine the evolution of the maximum and minimum values of nutrient concentration σ and tissue PSA concentration p for mild and aggressive tumors, respectively. It is noteworthy that, in all cases, the discrete MBP and discrete non-negative properties are perfectly preserved.

As depicted in Figure 1-12, our study not only successfully replicated the findings presented in the article [3] that described the original model but also performed MBP tests of the phase field equation and assessed the non-negativity of concentration, as depicted in Figures 13-16. In contrast, the simulation results in [3] did not maintain MBP and positivity at the numerical level. These three properties are of significant importance in the research, and ensure the smooth progression of our computational analyses. Consequently, our work contributes both theoretically and practically, providing novel perspectives and tools for further exploration in this field.

4.2. Simulation of PCa growth with treatment

In the subsequent simulations, we initially introduce the dosing regimen. The standard cytotoxic chemotherapy based on docetaxel typically involves up to 10 doses of the drug, administered every three weeks, which is mentioned in [3]. Our dosing times are denoted as $T_{c,i} = T_{a,i} = 60$, 81, 102, 123, 144, 165, 186, 207, 228, 249, i=1,...10, and we observe the outcomes up to T=365 days. Based on these dosing times, we classify the treatment regimens into three distinct groups for the purpose of simulation: (I) pure cytotoxic drugs, (II) pure anti-angiogenic drugs, and (III) a combination therapy regimen involving the administration of both drugs.

Figures 17-19 present simulations of aggressive tumor growth, nutrient diffusion, and PSA diffusion under three distinct drug-treatment strategies: (I) pure cytotoxic drugs, (II) pure anti-angiogenic drugs, and (III) combined therapy with both drugs. Additionally, Figure 20 illustrates the corresponding simulations of serum PSA levels and tumor volume for these three drug-treatment plans. The baseline case (a) of an aggressive tumor serves as a reference point for comparison. Our observations indicate that in the early stages, plans (I) and (III) were more effective in inhibiting tumor growth, resulting in a slower rate of tumor progression. As the number of drug injection cycles increased, plans (I) and (II) exhibited a tendency towards finger-like growth in the mid-term, while plan (III) maintained its spherical growth pattern. After 249 days, when drug injections were discontinued, the tumor had completely disappeared under plan (III), whereas tumors under plans (I) and (II) continued to grow, with plan (II) displaying slender finger-like growth. Comparing these results, we conclude that the combined therapy regimen under plan (III), consisting of both drugs, was the most effective. Under plan (I) of pure cytotoxic drug therapy, the tumor did not completely disappear in the later stages but was able to maintain its roughly spherical growth. Meanwhile, under plan (II) of pure

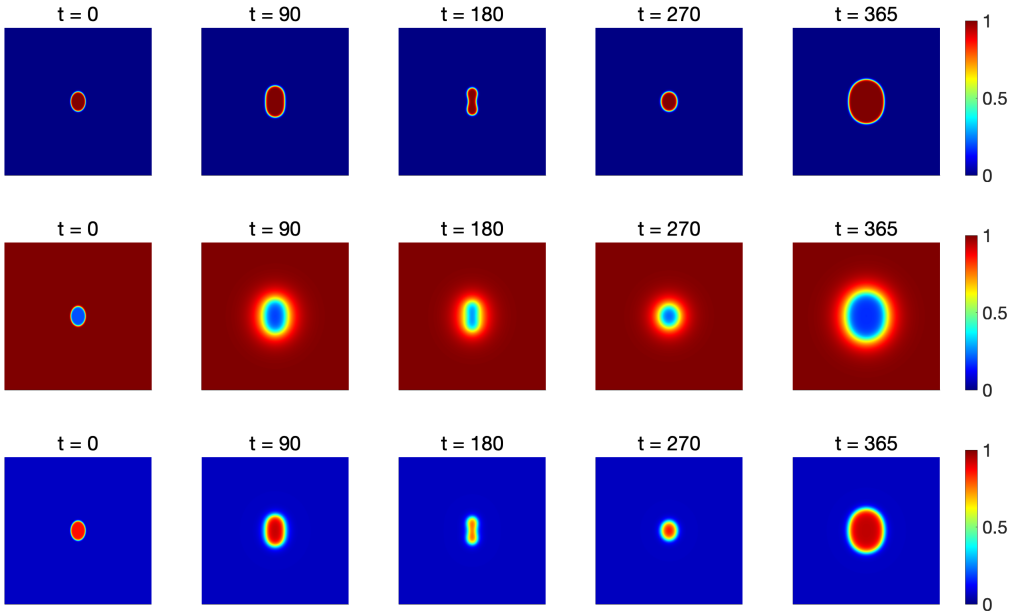

Figure 17: Tumor growth (the first row), Nutrient distribution (the second row) and PSA distribution (the third row) of an aggressive tumor with (I) pure cytotoxic drug therapy under baseline, with $S_c = 2.75$ and $\gamma_c = 17$.

anti-angiogenic drug therapy, the tumor still exhibited finger-like growth, indicating a potential for the tumor to become more aggressive.

For the case of PCa growth with treatment, our simulation results are not only consistent with the results presented in [3], but we also performed the MBP test of the phase-field equation and the non-negativity test for the two concentration parameters, as illustrated in Figure 21-22. These tests demonstrate that our algorithm can effectively maintain these three properties. This further validates the effectiveness of our approach in handling such problems. In summary, these simulations yield valuable insights into the behavior of both mild and aggressive tumors under various conditions. By examining the patterns of tumor growth, nutrient diffusion, and tissue PSA diffusion, we can enhance our understanding of how these factors influence tumor progression and potentially uncover novel treatment strategies.

5. Conclusion

In conclusion, our study presents a numerical approach for simulating the growth of PCa tumors and their response to drug therapy. This approach is based on a coupled system involving a phase field equation and two reaction-diffusion equations. We implemented fast second-order exponential time differencing Runge–Kutta schemes with stabilizing terms to ensure maximum bound principle on the order parameter and non-negativity of the concentration variables. These methods are decoupled, linear, explicit, and computationally efficient. Additionally, we employed fast algorithms based on the discrete cosine transform (DCT) and discrete sine transform (DST) using FFT-based techniques to solve the coupled phase field and reaction-diffusion equations with Dirichlet and Neumann boundary conditions in our numerical simulations. This enabled us to efficiently solve the coupled system over long periods of simulation time.

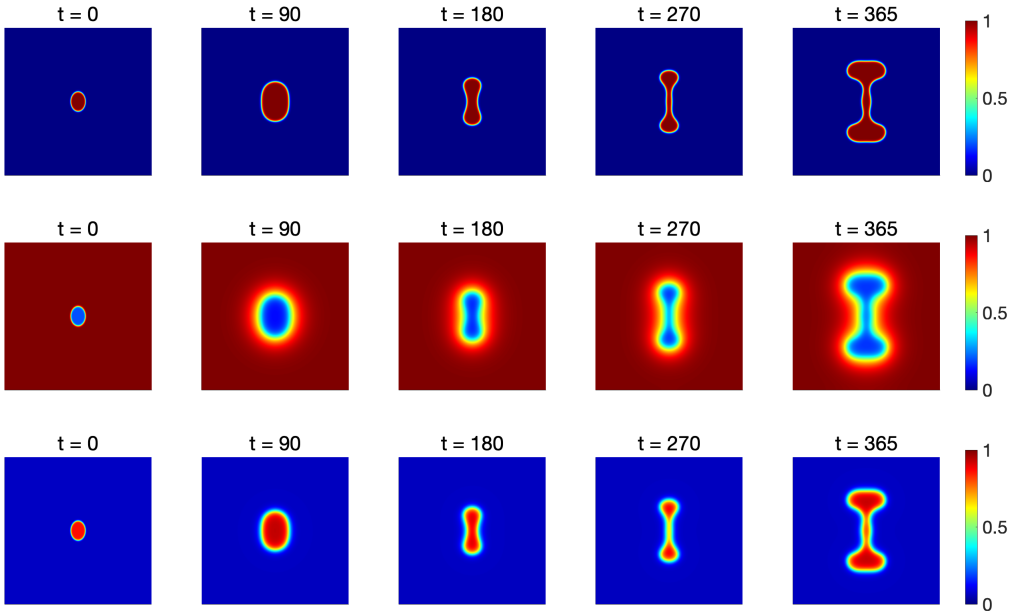

Figure 18: Tumor growth (the first row), Nutrient distribution (the second row) and PSA distribution (the third row) of an aggressive tumor with (II) pure anti-angiogenic drug therapy under baseline, with $S_c = 2.75$ and $\gamma_c = 17$.

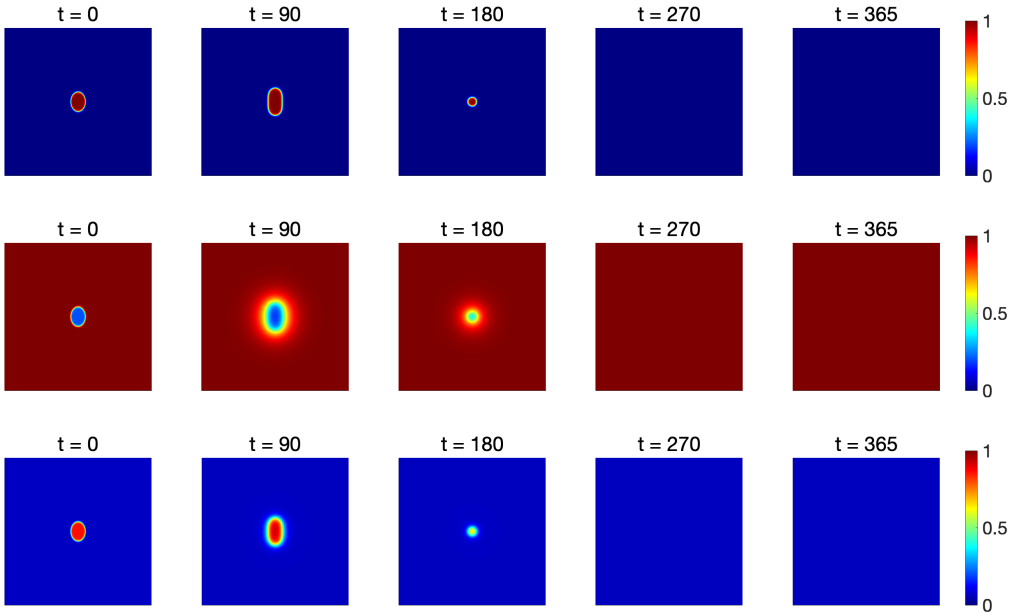

Figure 19: Tumor growth (the first row), Nutrient distribution (the second row) and PSA distribution (the third row) of an aggressive tumor with (III) combined therapy under baseline, with $S_c = 2.75$ and $\gamma_c = 17$.

The proposed methodologies enable us to make predictions regarding long-term tumor growth patterns and the outcomes of drug therapy, with simulations extending up

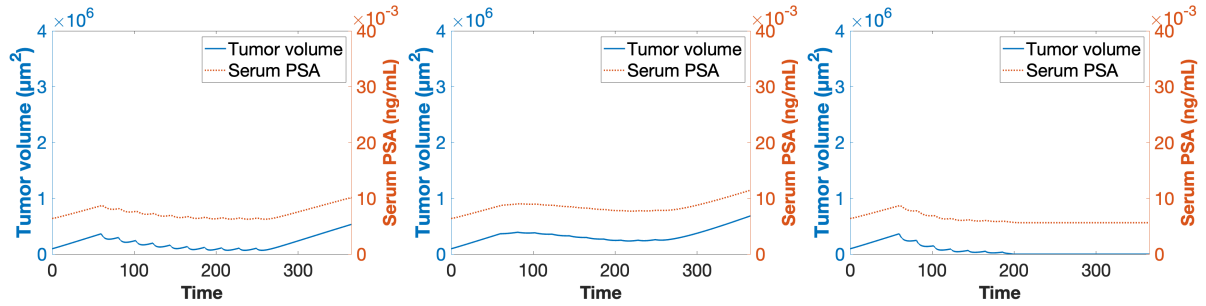

(a) baseline (b) higher nutrient (c) lower nutrient

Figure 20: Tumor volume and serum PSA of an aggressive tumor with treatment plans (I-III) underunder baseline parameters, with $S_c = 2.75$ and $\gamma_c = 17$.

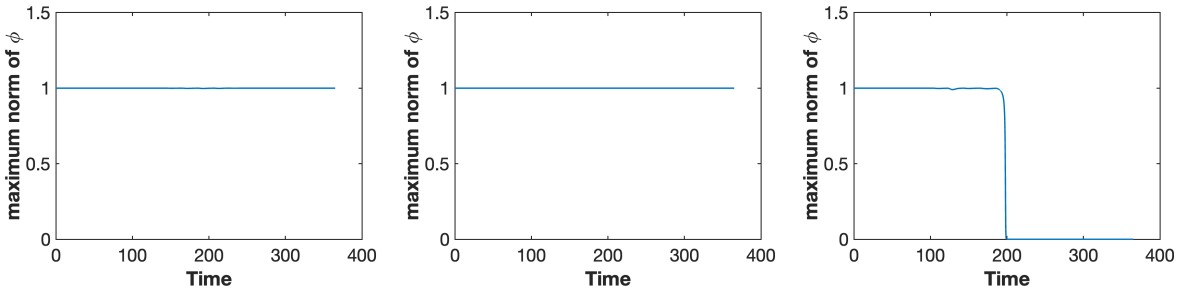

(a) baseline (b) higher nutrient (c) lower nutrient

Figure 21: MBP test of an aggressive tumor with treatment plans (I-III) under under baseline parameters, with $S_c = 2.75$ and $\gamma_c = 17$.

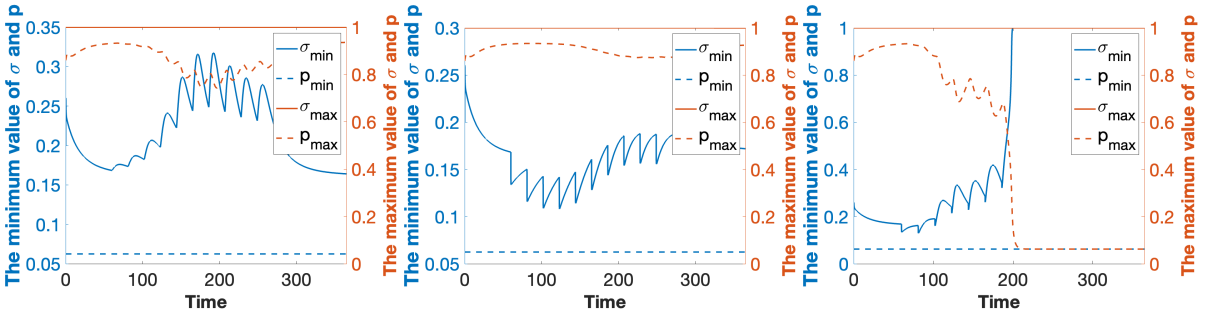

(a) baseline (b) higher nutrient (c) lower nutrient

Figure 22: Non-negative and bounded test of an aggressive tumor with treatment plans (I-III) under baseline parameters, with $S_c = 2.75$ and $\gamma_c = 17$.

to 365 days. By simulating both mild and aggressive tumors in different nutrient environments, we have successfully demonstrated the efficacy of our approach in forecasting tumor morphology and the temporal distribution of nutrient and PSA concentrations. Furthermore, we have conducted simulations to assess the impacts of three distinct drug treatments: pure cytotoxic drugs, pure anti-angiogenic drugs, and a combination therapy involving both cytotoxic and anti-angiogenic agents. Our findings indicate that the combined therapy yields the most favorable treatment outcomes.

This study presents a practical numerical framework for simulating tumor growth and predicting the results of drug therapy, thereby contributing to the field of cancer

research. The implications of our work extend to the design of more effective therapeutic interventions and a deeper comprehension of tumor growth patterns.

Future investigations could explore the application of our approach to other types of cancers, incorporating three-dimensional modeling and simulations, as well as investigating the potential of immunotherapy. These endeavors will serve to expand our understanding of cancer dynamics. Additionally, the exploration of multi-scale models will be crucial in obtaining a more comprehensive understanding of how various factors influence tumor growth. In conclusion, our research holds promise for informing the development of clinical treatment strategies for PCa and advancing our knowledge of tumor growth dynamics.

Acknowledgments

Q. Huang's work is supported by the National Natural Science Foundation of China (No. 11971047). Z. Qiao's work is supported in part by the Hong Kong Research Grants Council RFS grant RFS2021-5S03 and GRF grant 15302122, the Hong Kong Polytechnic University grant 4-ZZPF, and CAS AMSS-PolyU Joint Laboratory of Applied Mathematics.

References

[1] Sharyn D Baker, Ming Zhao, Carlton KK Lee, Jaap Verweij, Yelena Zabelina, Julie R Brahmer, Antonio C Wolff, Alex Sparreboom, and Michael A Carducci. Comparative pharmacokinetics of weekly and every-three-weeks docetaxel. *Clinical Cancer Research*, 10(6):1976–1983, 2004.

[2] Xiaowei Chen, Xu Qian, and Songhe Song. Fourth-order structure-preserving method for the conservative allen-cahn equation. *Advances in Applied Mathematics and Mechanics*, 15(1):159–181, 2023.

[3] Pierluigi Colli, Hector Gomez, Guillermo Lorenzo, Gabriela Marinoschi, Alessandro Reali, and Elisabetta Rocca. Mathematical analysis and simulation study of a phase-field model of prostate cancer growth with chemotherapy and antiangiogenic therapy effects. *Math. Models Methods Appl. Sci.*, 30(07):1253–1295, 2020.

[4] Qiang Du, Lili Ju, Xiao Li, and Zhonghua Qiao. Maximum principle preserving exponential time differencing schemes for the nonlocal Allen–Cahn equation. *SIAM J. Numer. Anal.*, 57(2):875–898, 2019.

[5] Qiang Du, Lili Ju, Xiao Li, and Zhonghua Qiao. Maximum bound principles for a class of semilinear parabolic equations and exponential time-differencing schemes. *SIAM Rev.*, 63(2):317–359, 2021.

[6] Jacques Ferlay, Isabelle Soerjomataram, Rajesh Dikshit, Sultan Eser, Colin Mathers, Marise Rebelo, Donald Maxwell Parkin, David Forman, and Freddie Bray. Cancer incidence and mortality worldwide: sources, methods and major patterns in globocan 2012. *International journal of cancer*, 136(5):E359–E386, 2015.

[7] Zhongxiong Gao, Hong Zhang, Xu Qian, and Songhe Song. High-order unconditionally maximum-principle-preserving parametric integrating factor Runge-Kutta schemes for nonlocal Allen–Cahn equation. *Applied Numerical Mathematics*, 194:97–114, 2023.

[8] Philip Hahnfeldt, Judah Folkman, and Lynn Hlatky. Minimizing long-term tumor burden: the logic for metronomic chemotherapeutic dosing and its antiangiogenic basis. *Journal of theoretical biology*, 220(4):545–554, 2003.

[9] Ville Härmä, Johannes Virtanen, Rami Mäkelä, Antti Happonen, John-Patrick Mpindi, Matias Knuuttila, Pekka Kohonen, Jyrki Lötjönen, Olli Kallioniemi, and Matthias Nees. A comprehensive panel of three-dimensional models for studies of prostate cancer growth, invasion and drug responses. *PloS one*, 5(5):e10431, 2010.

[10] Peter Hinow, Philip Gerlee, Lisa J McCawley, Vito Quaranta, Madalina Ciobanu, Shizhen Wang, Jason M Graham, Bruce P Ayati, Jonathan Claridge, Kristin R Swanson, et al. A spatial model of tumor-host interaction: application of chemotherapy. *Mathematical biosciences and engineering: MBE*, 6(3):521, 2009.

[11] Dianming Hou, Lili Ju, and Zhonghua Qiao. A linear second-order maximum bound principle-preserving BDF scheme for the Allen–Cahn equation with a general mobility. *Math. Comp.*, 92(344):2515–2542, 2023.

[12] Dianming Hou and Zhonghua Qiao. An implicit-explicit second-order BDF numerical scheme with variable steps for gradient flows. *J. Sci. Comput.*, 94(2):Paper No. 39, 22, 2023.

[13] Tianliang Hou, Tao Tang, and Jiang Yang. Numerical analysis of fully discretized crank–nicolson scheme for fractional-in-space Allen–Cahn equations. *Journal of Scientific Computing*, 72:1214–1231, 2017.

[14] Lili Ju, Xiao Li, and Zhonghua Qiao. Generalized SAV-exponential integrator schemes for Allen-Cahn type gradient flows. *SIAM J. Numer. Anal.*, 60(4):1905–1931, 2022.

[15] Lili Ju, Xiao Li, and Zhonghua Qiao. Stabilized exponential-SAV schemes preserving energy dissipation law and maximum bound principle for the Allen-Cahn type equations. *J. Sci. Comput.*, 92(2):Paper No. 66, 34, 2022.

[16] Lili Ju, Xiao Li, Zhonghua Qiao, and Jiang Yang. Maximum bound principle preserving integrating factorRunge–Kutta methods for semilinear parabolic equations. *J. Comput. Phys.*, 439:110405, 2021.

[17] Lili Ju, Jian Zhang, Liyong Zhu, and Qiang Du. Fast explicit integration factor methods for semilinear parabolic equations. *J. Sci. Comput.*, 62(2):431–455, 2015.

[18] Jingwei Li, Xiao Li, Lili Ju, and Xinlong Feng. Stabilized integrating factor runge–kutta method and unconditional preservation of maximum bound principle. *SIAM Journal on Scientific Computing*, 43(3):A1780–A1802, 2021.

[19] Hans Lilja, David Ulmert, and Andrew J Vickers. Prostate-specific antigen and prostate cancer: prediction, detection and monitoring. *Nat. Rev. Cancer*, 8(4):268–278, 2008.

[20] Guillermo Lorenzo, Thomas JR Hughes, Pablo Dominguez-Frojan, Alessandro Reali, and Hector Gomez. Computer simulations suggest that prostate enlargement due to mechanically impedes prostate cancer growth. *Proc. Natl. Acad. Sci.*, 116(4):1152–1161, 2019.

[21] Guillermo Lorenzo, Michael A Scott, Kevin Tew, Thomas JR Hughes, Yongjie Jessica Zhang, Lei Liu, Guillermo Vilanova, and Hector Gomez. Tissue-scale, personalized modeling and simulation of prostate cancer growth. *Proc. Natl. Acad. Sci.*, 113(48):E7663–E7671, 2016.

[22] Min Jhe Lu, Wenrui Hao, Chun Liu, John Lowengrub, and Shuwang Li. Nonlinear simulation of vascular tumor growth with chemotaxis and the control of necrosis. *J. Comput. Phys.*, 459:111153, 2022.

[23] Rita Mehta, Ainura Kyshtoobayeva, Tom Kurosaki, Eric J Small, Hun Kim, Robert Stroup, Christine E McLaren, Kuo-Tung Li, and John P Fruehauf. Independent association of angiogenesis index with outcome in prostate cancer. *Clinical cancer research*, 7(1):81–88, 2001.

[24] Vahid Mohammadi and Mehdi Dehghan. Simulation of the phase field Cahn–Hilliard and tumor growth models via a numerical scheme: element-free Galerkin method. *Comput. Meth. Appl. Mech. Eng.*, 345:919–950, 2019.

[25] Vahid Mohammadi, Mehdi Dehghan, and Stefano De Marchi. Numerical simulation of a prostate tumor growth model by the RBF-FD scheme and a semi-implicit time discretization. *J. Comput. Appl. Math.*, 388:113314, 2021.

[26] Niusha Narimani and Mehdi Dehghan. Predicting the effect of a combination drug therapy on the prostate tumor growth via an improvement of a direct radial basis function partition of unity technique for a diffuse-interface model. *Comput. Biol. Med.*, 157:106708, 2023.

[27] Kenneth J Pienta and David C Smith. Advances in Prostate Cancer Chemotherapy: A New Era Begins 1. *Ca-Cancer J. Clin.*, 55(5):300–318, 2005.

[28] G Powathil, M Kohandel, S Sivaloganathan, A Oza, and M Milosevic. Mathematical modeling of brain tumors: effects of radiotherapy and chemotherapy. *Physics in Medicine & Biology*, 52(11):3291, 2007.

[29] Bostjan Seruga and Ian F Tannock. Chemotherapy-based treatment for castration-resistant prostate cancer. *Journal of clinical oncology*, 29(27):3686–3694, 2011.

[30] Jie Shen, Tao Tang, and Jiang Yang. On the maximum principle preserving schemes for the generalized Allen–Cahn equation. *Communications in Mathematical Sciences*, 14(6):1517–1534, 2016.

[31] Xiaoqin Shen, Lixiao Wu, Juan Wen, and Juan Zhang. SAV Fourier-spectral method for diffuse-interface tumor-growth model. *Comput. Math. Appl.*, 140:250–259, 2023.

[32] Rebecca L Siegel, Kimberly D Miller, Nikita Sandeep Wagle, and Ahmedin Jemal. Cancer statistics, 2023. *Ca-Cancer J. Clin.*, 73(1):17–48, 2023.

[33] Tao Tang and Jiang Yang. Implicit-explicit scheme for the Allen–Cahn equation preserves the maximum principle. *Journal of Computational Mathematics*, pages 451–461, 2016.

[34] Albert J ten Tije, Jaap Verweij, Michael A Carducci, Wilfried Graveland, Theresa Rogers, Tatjana Pronk, MP Verbruggen, Fitzroy Dawkins, and Sharyn D Baker. Prospective evaluation of the pharmacokinetics and toxicity profile of docetaxel in the elderly. *Journal of Clinical Oncology*, 23(6):1070–1077, 2005.

[35] Charles Van Loan. *Computational Frameworks for the Fast Fourier Transform*. SIAM, 1992.

[36] Noel Weidner, PR Carroll, J Flax, W_ Blumenfeld, and J Folkman. Tumor angiogenesis correlates with metastasis in invasive prostate carcinoma. *The American journal of pathology*, 143(2):401, 1993.

[37] Steven M Wise, John S Lowengrub, Hermann B Frieboes, and Vittorio Cristini. Three-dimensional multispecies nonlinear tumor growth—I: model and numerical method. *J. Theor. Biol.*, 253(3):524–543, 2008.

[38] Jiangping Xu, Guillermo Vilanova, and Hector Gomez. A mathematical model coupling tumor growth and angiogenesis. *PloS one*, 11(2):e0149422, 2016.